

Processes that influence sea surface temperature and ocean mixed layer depth variability in a coupled model

Michael A. Alexander*

James D. Scott

*NOAA-CIRES/Climate Diagnostics Center
University of Colorado*

Clara Deser

National Center for Atmospheric Research

(Submitted to the Journal of Geophysical Research: Oceans)

March 1999

Accepted March 2000

*Corresponding author address:

Dr. Michael Alexander

NOAA-CIRES/Climate Diagnostics Center

R/E/CDC1

325 Broadway

Boulder, CO 80303-3328

ABSTRACT

A 50-year coupled atmosphere-ocean model integration is used to study sea surface temperature (SST) and mixed layer depth (h), and the processes which influence them. The model consists of an atmospheric general circulation model coupled to an ocean mixed layer model in ice-free regions. The midlatitude SST variability is simulated fairly well, although the maximum variance is underestimated and located farther south than observed. The model is clearly deficient in the vicinity of the Gulf Stream and in the eastern tropical Pacific where advective processes are important. The model generally reproduces the observed structure of the mean h in both March and September but underestimates it in the North Atlantic during winter. The net surface heat flux strongly regulates both the mean ($\bar{}$) and the anomalous (δ) SSTs throughout the year. The entrainment heat flux, which is proportional to the product of the entrainment rate (W_e) and the temperature jump at the base of the mixed layer (ΔT), influences SSTs in summer and fall, especially north of $\sim 35^\circ\text{N}$ (45°N) in the Pacific (Atlantic). $\overline{W_e \Delta T}$ is more important for the development of (SST') in fall compared to $W_e \overline{\Delta T}$, which is larger in summer. The entrainment rate is dominated by wind-induced mixing in summer and surface buoyancy forcing in winter; the density jump at the base of the mixed layer is of secondary importance. In addition, anomalies in h have a significant impact on the heat balance of the mixed layer during spring and summer. Deep winter mixed layers and the storage of thermal anomalies beneath the shallow mixed layer in summer leads to large winter-to-winter persistence of SST anomalies in the far North Atlantic, in accord with observations and stochastic climate theory.

1. Introduction

Beginning with the pioneering work of *Namias* [1959, 1963] and *Bjerknes* [1964], numerous studies have sought to understand how midlatitude sea surface temperature (SST) anomalies form and the extent to which they influence the atmosphere. SST anomalies may form through changes in air-sea heat fluxes, horizontal and vertical ocean heat transport, and turbulent mixing. Many of the early studies [see *Frankignoul*, 1985], focused on the role of advection: [*Namias*, 1959, 1965] found that anomalous Ekman drift played an important role in generating SST anomalies, while *Jacob* [1967], *Namias* [1972], and *Favorite and McClain* [1973] suggested that the mean advection of anomalous temperatures could also be important. More recent modeling studies confirmed that anomalous Ekman transport could help to create SST anomalies in regions of strong SST gradients [*Haney*, 1980; *Luksch and von Storch*, 1992; *Miller et al.*, 1994; *Luksch*, 1996]. However, on timescales of less than ~10 years, most studies have found that surface heat fluxes play a dominant role in forcing midlatitude SST anomalies [*Gill and Niiler*, 1973; *Salmon and Hendershott*, 1976; *Frankignoul and Reynolds*, 1983; *Battisti et al.*, 1995; *Halliwel and Mayer*, 1996], while Ekman pumping plays a negligible role [*White et al.*, 1980; *Haney et al.*, 1983; *Schneider et al.*, 1999].

High-resolution measurements of currents, temperature, and indicate that upper ocean processes, in addition to surface heat fluxes, can have an important impact on SSTs [e.g., *Davis et al.*, 1981; *Large et al.*, 1986; *Webster and Lukas*, 1992]. However, most field studies are of short duration, generally lasting less than a few months. Longer records, of the order of 20-40 years, are available from a few of the ocean weather ships stationed in the North Atlantic and Pacific Oceans. Using weather ship data, *Clark* [1972], *Elsberry and Garwood* [1980], and *Lanzante and Harnack* [1983] found that the anomalies in the depth of the well mixed surface layer could significantly influence SSTs in spring and summer. *Camp and Elsberry* [1978] showed that cooling due to entrainment of subsurface water into the mixed layer could be an order of magnitude larger than the surface energy fluxes during the passage of storms at weather ship *P* (50°N, 145°W). *Namias and Born* [1970, 1974] and *Alexander and Deser* [1995] presented evidence that thermal anomalies created in the deep ocean mixed layer could remain intact in the seasonal thermocline (30-100 m) during summer and return to the surface layer in the following fall and winter. However, many upper ocean processes, such as entrainment, and their impact on SST are very difficult to measure directly.

A wide variety of models have been employed to study the role of the oceans in climate, ranging from fixed depth slabs to ocean general circulation models (GCMs). Intermediate models, including bulk mixed layer and one-dimensional layered models have proven to be useful for studying vertical processes in the upper ocean [e.g., *Garwood*, 1977; *Niiler and Kraus*, 1977; *Price et al.*, 1986; *Kantha and Clayson*, 1994; *Large et al.*, 1994]. In bulk models the temperature (and salinity and currents if included) is predicted for the mixed layer as a whole, and the mixed layer depth (h) depends on processes that create turbulence, including mechanical mixing by wind stress and convective mixing by the surface buoyancy flux. Bulk models appear to be as accurate in their simulation of SST and h as more sophisticated and computationally intensive layered models [*Martin*, 1985; *Gaspar et al.*, 1988; *Kraus*, 1988]. However, both types of models have generally been developed and tested at only a few weather ship locations, and bulk models cannot reproduce the detailed vertical structure of turbulence. Bulk models have been used to study the mean seasonal cycle of SST and h [*Gordon and Bottomly*, 1985; *Le Treut et al.*, 1985; *Simonot et al.*, 1988] and the formation of SST anomalies over the North Pacific [*Miyakoda and Rosatti*, 1984; *Alexander*, 1992] and North Atlantic [*Battisti et al.*, 1995]. In addition, the surface layer in isopycnal ocean GCMs, is parameterized using a bulk mixed layer model [*Oberhuber* 1993; *New et al.*, 1995].

Ocean mixed layer models are also useful for understanding the processes that contribute to the variability of SST and h over the course of the seasonal cycle. *Alexander and Penland* [1996] used a statistical atmospheric model, based on observations from weather ship *P*, to drive a mixed layer ocean model. The model provided a reasonable estimate of the range of the mean and standard deviation of upper ocean temperature and mixed layer depth over the seasonal cycle. An analysis of the temperature tendency indicated that anomalies in the net heat flux, mixed layer depth, and entrainment heat flux all provided a significant contribution to the growth of SST anomalies at different times of the year. Anomalies in h were highly correlated with the surface buoyancy flux in winter and the surface wind stress in summer.

The seasonal cycle and horizontal variability of h is also critical to the subduction of water into the permanent thermocline via lateral induction, the advection of surface water through the sloping base of the winter mixed layer [*Woods* 1985; *Marshall et al.*, 1993; *New et al.* 1995; *Inui et al.* 1999]. Recently, *Ladd and Thompson* [1999] used mixed layer model simulations to examine the role of one-dimensional processes in the formation of mode water, a thick homogeneous layer

created by subduction. They found that surface buoyancy forcing played a critical role in mode water development in the central and east Pacific by influencing the depth of the mixed layer in winter and the strength of the seasonal pycnocline in summer.

In the present study, we examine the processes that influence SST and h using an atmospheric GCM coupled to a grid of one-dimensional mixed layer ocean models. Most previous studies of mixed layer variability have been limited in area and/or duration; those modeling studies that have been on the regional-to-global scale have focused on reproducing the observed mean seasonal cycle of SST and h . Here in addition to documenting the fidelity of the ocean model, we examine the influence of vertical processes on both the mean and the anomalous SSTs over the extratropical Northern Hemisphere oceans. We find that anomalies in mixed layer depth and the entrainment of subsurface water into the mixed layer impact the development of SST anomalies in spring and fall, respectively. We document the winter-to-winter SST autocorrelations in the model and the observations and present a simple physical interpretation of the results. We also examine the interannual variability of h and the relative roles of buoyancy forcing, wind stirring, and stratification of the upper ocean on the evolution of mixed layer depth over the seasonal cycle. Our goal is to extend the findings of previous theoretical and limited area studies to investigate mixed layer physics over a broad range of conditions in the North Atlantic and Pacific during the course of the seasonal cycle. We find that the entrainment rate is generally dominated by wind-induced mixing in summer and buoyancy forcing in winter; the stratification is generally of secondary importance. In addition, a detailed examination of the magnitude of the two scaling parameters, which control mixing efficiency, indicates that entrainment is primarily controlled by mechanical/buoyancy forcing (Monin-Obukhov scale) rather than by rotation (Ekman scale).

Results from stand-alone ocean model simulations strongly depend on the choice of surface boundary conditions. For example, using observed surface air temperatures and the simulated SSTs to compute the surface heat fluxes strongly constrains the upper ocean temperature to follow observations, while models driven by fluxes determined completely from observations can drift from the observed climate [Frankignoul, 1985; Alexander and Deser 1995]. By using a coupled model we avoid the very difficult task of finding the appropriate boundary conditions to drive an ocean model. The AGCM also provides global surface fields without spatial or temporal gaps or spurious trends. Finally, given that a coupled AGCM-mixed layer model system does not include ENSO dynamics, we are able to isolate how internal atmospheric variability, thermodynamic air-sea

coupling, and mixed layer physics influence SST variability.

The atmosphere, ocean, and ice components of the coupled model, the initial model state, the method of coupling, and the surface flux correction are described in section 2. The mean and standard deviation of SST and h during March and September, the peak of winter and summer in the northern oceans, are discussed in section 3. Factors that control the mean and anomalous SST tendency and the winter-to-winter correlation of SST anomalies are examined in sections 4 and 5. The relationships between the entrainment rate with the shear and buoyancy forcing are explored in section 6. The results are summarized and discussed in section 7.

2. Coupled Model

A 50-year simulation with a global coupled atmosphere-ocean model is used to study upper ocean variability in the northern midlatitude oceans. The model consists of a Geophysical Fluid Dynamics Lab (GFDL) atmospheric general circulation model (AGCM) connected to an upper ocean mixed layer model (MLM). Alexander and Deser [1995], Battisti et al. [1995], Alexander and Penland [1996], and Bhatt et al. [1998] have used a slightly different version of the MLM to study upper ocean processes and midlatitude air-sea interaction. The ocean model consists of a grid of independent column models which include local atmosphere-ocean fluxes and the turbulent entrainment of water into the surface mixed layer, but not mean vertical motions or horizontal processes. The ocean column models are aligned with the AGCM grid over ice free regions of the global oceans. In regions with sea ice, the ice fraction, ice thickness, and SST are specified.

2.1 Atmospheric Model

The GFDL AGCM is a global spectral model with rhomboidal truncation at wave number 30, which is approximately 2.25° latitude by 3.75° longitude. The model has 14 unequally spaced sigma levels in the vertical, with the lowest level at ~ 30 m above the surface. The model includes smoothed topography, gravity wave drag, and predicted clouds and soil moisture. Stratiform clouds form and precipitation occurs when the relative humidity exceeds 100%, while subgrid scale precipitation is parameterized by moist convective adjustment. Many features of the model's climate are presented on the World Wide Web [Alexander and Scott, 2000], while a more complete description of an earlier version of the GCM is given by Gordon and Stern [1982] and Manabe and Hahn [1981].

2.2. Mixed Layer Ocean Model

The individual column models consist of a uniform mixed layer atop a layered model that represents conditions in the pycnocline. Here we use the model developed by *Gaspar* [1988], which has been formulated with climate simulations in mind. The temperature tendency of the mixed layer is given by

$$\frac{\partial T_m}{\partial t} = \frac{Q_{net} + Q_{cor}}{\rho c h} - \frac{Q_{sw h}}{\rho c h} + \frac{W_e \Delta T}{h} + CA - \frac{\kappa \partial T}{h \partial z} \Big|_{z=-h} \quad (1)$$

where T_m is the mixed layer temperature, $\Delta T = T_b - T_m$, T_b is the temperature of the remainder of the layer below h , Q_{net} is the net surface energy flux into the ocean, Q_{cor} is the surface heat flux correction, $Q_{sw h}$ is the penetrating solar radiation at h , W_e the entrainment rate, ρ and c are the reference density and specific heat of sea water, κ is the diffusion coefficient for small-scale motion, and z is the vertical coordinate. Convective adjustment (CA) occurs when the mixed layer is more dense than the layer below; at that time, heat within the remainder of the layer below h is incorporated into the mixed layer and h is then set to the top of the next layer. The model has a similar predictive equation for mixed layer salinity, where the freshwater flux is due to precipitation - evaporation ($P-E$).

The mixed layer depth primarily increases via entrainment, except in high latitudes where h can significantly deepen via CA . By vertically integrating the turbulent kinetic energy equation over h and then applying a fairly standard set of assumptions [see Niiler and Krauss, 1977], W_e can be expressed as:

$$W_e = \frac{m u_*^3 - 0.5 h B(h) - h \epsilon}{h \Delta b + q^2} \quad (2)$$

where m is a constant, the surface friction velocity $u_* = \sqrt{\tau/\rho}$, where τ is the surface wind stress, and Δb is the buoyancy jump at the base of the mixed layer; following *Gaspar* [1988], equation (2) neglects mixing due to current shear across the base of the mixed layer. The buoyancy flux integrated over the mixed layer ($B(h)$) depends on Q_{net} , $P-E$, and the absorption of solar radiation in the water column. The mean turbulent kinetic energy (q^2), which is usually small but can be important for near neutral conditions, is parameterized following *Kim* [1976]. Mixed layer models generally differ in their parameterization of ϵ , the turbulent dissipation rate; here we use the formulation and parameter values given by *Gaspar* [1988]. When deepening by entrain-

ment, h is computed as a prognostic variable ($\frac{\partial h}{\partial t} = W_e$).

When shoaling, the mixed layer reforms closer to the surface, W_e is set to zero, and h is computed as a diagnostic quantity by assuming a balance between wind stirring, buoyancy forcing, and dissipation. When the mixed layer shoals, the temperature (salinity) profile is adjusted to conserve heat (salt) and the temperature (salinity) change at the base of the mixed layer. The prognostic equations for T_m , S_m , and h are integrated using a first-order forward in time scheme.

The region beneath the mixed-layer is represented by a multi-layer system, where the temperature and salinity of the layers change by convective adjustment, vertical diffusion, and linear damping. The temperature of the upper 300 m can also change due to penetrating solar radiation. The vertical diffusion is calculated using the Crank-Nicholson scheme with a constant diffusion coefficient of $1.0 \times 10^{-5} \text{ m}^2 \text{ s}^{-2}$, a value suggested by the tracer experiments of *Ledwell et al.* [1993]. The temperature and salinity in all model layers are damped toward their monthly mean climatological values on a 10-year timescale. This weak, Newtonian damping, which crudely represents processes that vary with depth such as the mean heat transport, was necessary for the model to retain a stable density profile in regions of strong current shear. The absorption of solar radiation is parameterized following *Paulson and Simpson* [1977].

The bottom of the MLM is 1000 m or the actual ocean depth, whichever is smaller. For open ocean points, the MLM contains 31 unequally spaced layers between the surface and 1000 m, where 15 of the layers are within the first 100 m, and the temperature and salinity of the final layer is set to the observed climatological value. The mixed layer depth is not forced to coincide with the levels of the layered model; the temperature of layers that are entirely above h are set to T_m while T_b is from the remainder of the layer which is beneath h . However, h is constrained to be greater than 10 m and less than 850 m or the bottom of the ocean, whichever is smaller.

2.3. Sea Ice

For points where sea ice occurs during any part of the mean seasonal cycle, the MLM is not active; instead, the daily ice thickness and ice fraction (or SST during ice-free periods) are specified on the basis of the interpolated monthly mean climatology for the period 1950-1995. Heat fluxes in these areas are weighted for the appropriate proportions of open water and ice. Sea ice can also form over the active MLM points, which are beyond the maximum extent of climatological ice when

T_m drops to the freezing point for seawater, 271.16 K. A simple heat balance model is used for the ice, which is assumed to cover 100% of the grid box.

2.4. Air-Sea Coupling and Surface Heat Flux Correction

Heat, momentum, and freshwater are exchanged across the model's air-sea interface. The net heat flux consists of the shortwave, longwave, sensible, and latent heat flux. The radiative fluxes in the AGCM depend on temperature, water vapor, clouds, and specified trace constituents. The sensible and latent heat flux are computed using standard bulk aerodynamic formulas where the exchange coefficients have a constant value of 1.0×10^{-3} . The surface wind stress is computed in a similar fashion. The wind speed, air temperature, and specific humidity used in the bulk formulas are taken directly from the lowest model level of the AGCM, while the SST is given by T_m obtained from the ocean model. The atmosphere and ocean models exchange information once per day, the time step of the MLM. The atmosphere-to-ocean fluxes are averaged over the 96 time steps in one AGCM day, while the ocean-to-atmosphere fluxes are computed every AGCM time step using the daily SST values.

Because of errors in the surface fluxes and processes absent from the ocean model it is necessary to correct the surface fluxes in order to prevent climate drift. *Sausen et al.* [1988] showed that model drift can affect how the climate responds to perturbations, such as SST anomalies or the doubling of CO_2 . Flux corrections have been used in models ranging from slabs to GCMs [e.g., *Sausen and Ponater*, 1998; *Manabe and Stouffer*, 1988; *Battisti et al.*, 1995; *Gordon and O'Farrell*, 1997]. Here surface flux correction values are computed such that the mean seasonal cycle of SSTs and salinity simu-

lated by the mixed layer closely follow observations. The flux corrections vary with location and time of year but do not vary from one year to the next.

The surface heat and salt flux corrections are obtained from a 20-year MLM simulation using surface fluxes from an independent GFDL AGCM run, where the AGCM had observed climatological SSTs as boundary conditions. The daily SSTs used in the AGCM simulation were obtained by interpolating the long-term monthly values from the *Smith et al.* [1996] data set. Prior to each time step, the SSTs in the 20-year MLM simulation are set to the observed climatological values, which are also the SST boundary condition for the AGCM on that day. The MLM is then run for one time step (one day) where T_m and h are free to evolve. At each ocean model grid point, the heat flux correction is computed such that the T_m predicted by the MLM

matches the observed SST at the next time step. A similar method is used to obtain the salt flux correction. This procedure is repeated each day to obtain 20 years of daily flux correction values. Long-term monthly mean corrections are computed and then linearly interpolated to daily values. The daily correction values are then added as a forcing term to the temperature and salinity tendency equations in the 50-year coupled run but are not included when computing W_e and h .

The annual mean surface heat flux correction Q_{cor} is shown in Figure 1 for the North Atlantic and Pacific Oceans. Heat is added to the oceans in the western $\sim 1/2$ of both basins, with maxima of $\sim 150 \text{ W m}^{-2}$ to the east of Japan and the east coast of the United States. The magnitude and pattern of $-Q_{cor}$ resembles the observed annual mean Q_{net} and equivalently the mean oceanic heat flux convergence [*Hsuung*, 1985; *Moisan and Niiler*, 1998], indicating that the correction is primarily accounting for the absence of advection in the ocean

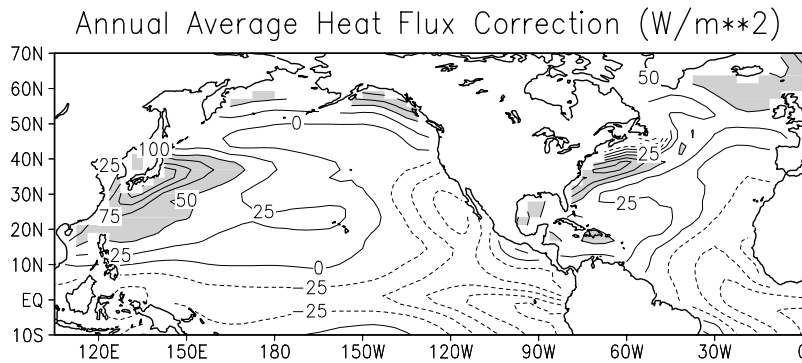


Fig. 1. Annual average surface heat flux correction (W m^{-2}). Positive values indicate heat is added to the ocean. The contour interval is 25 and values greater than 50 are shaded. This figure and all subsequent planar plots have been smoothed using a 9-point filter.

model. Q_{cor} exceeds 300 W m^{-2} in the vicinity of the Kuroshio Current and Gulf Stream in March but is negligible in September (not shown), due to the large seasonal cycle in heat transported by these current systems [Wilkin *et al.*, 1995; Yu and Malanotte-Rizzoli, 1998]. The GFDL AGCM, like many current climate models, overestimates the shortwave radiation reaching the surface, primarily due to errors in simulating clouds [Garrott *et al.*, 1998]. As a result, Q_{cor} values between -50 and -100 W m^{-2} are applied to the MLM during summer from 40°N to 60°N .

2.5. Initial Conditions

The initial ocean conditions for the coupled model integration were derived by averaging the MLM variables on January 1 for 20 years of an MLM simulation driven by surface fluxes from a previous AGCM simula-

tion. The atmospheric conditions were obtained for January 1 by integrating the GFDL AGCM for five years beginning from a state of rest. Since the AGCM and MLM initial conditions were obtained independently, there is an adjustment period of a few months once the two models are coupled.

3. SST and h

Here we examine sea surface temperature and mixed layer depth fields from the 50-year coupled atmosphere-ocean integration and compare them to observations. The simulated and observed long-term monthly mean SST differ by less than 1°C at nearly all of the MLM grid points (not shown), a result of imposing a surface flux correction. However, these small differences are systematic: the simulated SSTs tend to be too warm (cold) in summer (winter). These model biases are due to nonlinearities in the MLM, computing the

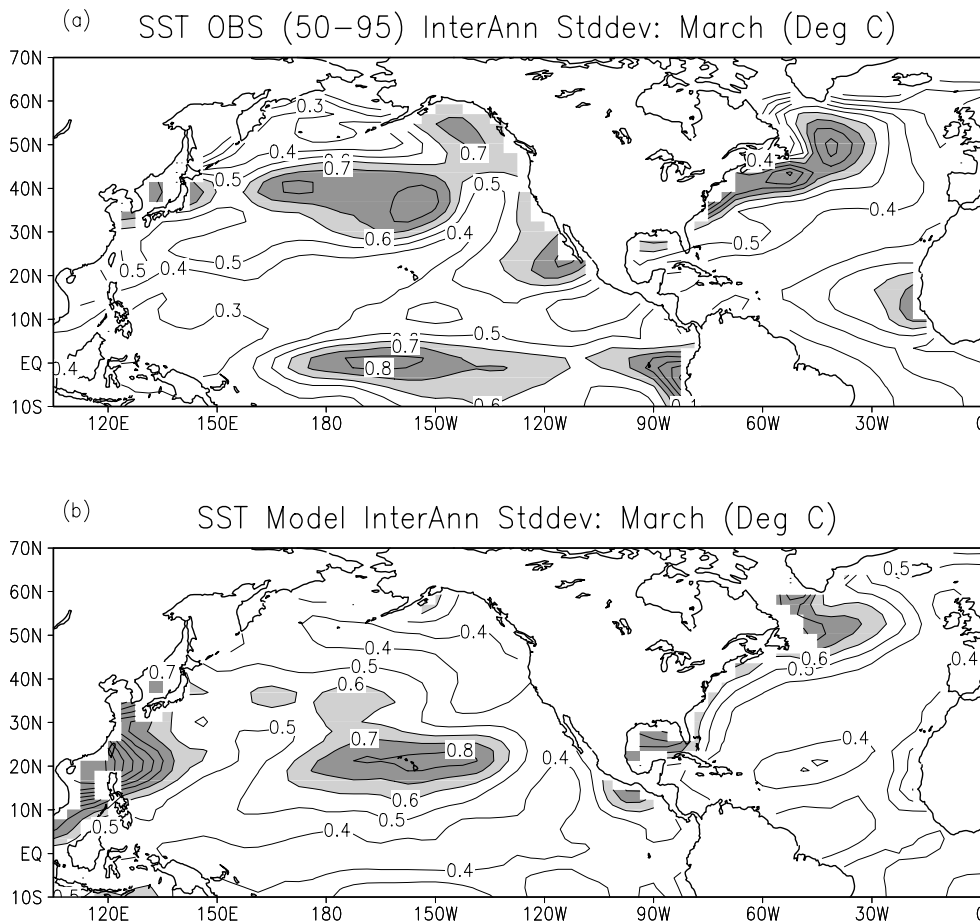


Fig. 2. The standard deviation (σ) of March SSTs ($^\circ\text{C}$) from (a) observations and (b) the 50-year coupled model simulation. The observed SSTs, which extend from 1950-95, are originally from the data set of Smith *et al.* (1996) which have then been interpolated from a $2^\circ \times 2^\circ$ grid to the R30 Gaussian grid. The contour interval is 0.1°C , and $0.6^\circ\text{C} < \text{SST} < 0.8^\circ\text{C}$ is shaded light while those greater than 0.7°C are shaded dark.

flux corrections from a 20-year ocean only integration, and the method used to interpolate the flux corrections in time did not preserve the monthly means from which they were computed.

The observed and simulated interannual standard deviations (σ) of SST in March over the Northern Hemisphere oceans are shown in Figure 2. The standard deviations are computed from the departures of the individual monthly means from the long-term monthly means. The observed σ values are derived from the *Smith et al.* [1996] data set for the period 1950-1995, while the simulated values are from the 50-year model integration. Both the simulated and the observed σ range from 0.3° to 1.2°C over the open ocean. In the Atlantic, σ is maximized along the east coast of North America, in part due to the variability in wind speed and air temperature associated with continental air masses moving over the ocean. However, only the observations exhibit a band of enhanced σ that extends from the mid-Atlantic states to east of Newfoundland, which probably arise due to variability in Ekman transport across strong

SST gradients [Luksch, 1996] and in heat transport by the Gulf Stream and North Atlantic Current. The March σ exceeds 0.6°C in the central North Pacific in both the model and observations, but the maximum variability of $\sim 0.8^\circ\text{C}$ occurs 10°-15° farther south in the model. The simulated SST variability is also greater (less) than observed in the South China Sea (Gulf of Alaska). Since the coupled model does not contain horizontal processes such as currents and wave dynamics, there is no El Niño-Southern Oscillation (ENSO), and σ is significantly underestimated in the eastern tropical Pacific (Figure 2).

Fluctuations in the strength and position of the Aleutian low associated with ENSO have been shown to cause SST anomalies to form in the North Pacific primarily through changes in Q_{net} [Alexander, 1992; Luksch and von Storch, 1992; Lau and Nath, 1996]. We have examined the influence of ENSO on midlatitude SSTs using an additional GFDL AGCM-MLM experiment where observed SSTs are specified between approximately 25°N and 25°S in the Pacific for the period 1950-

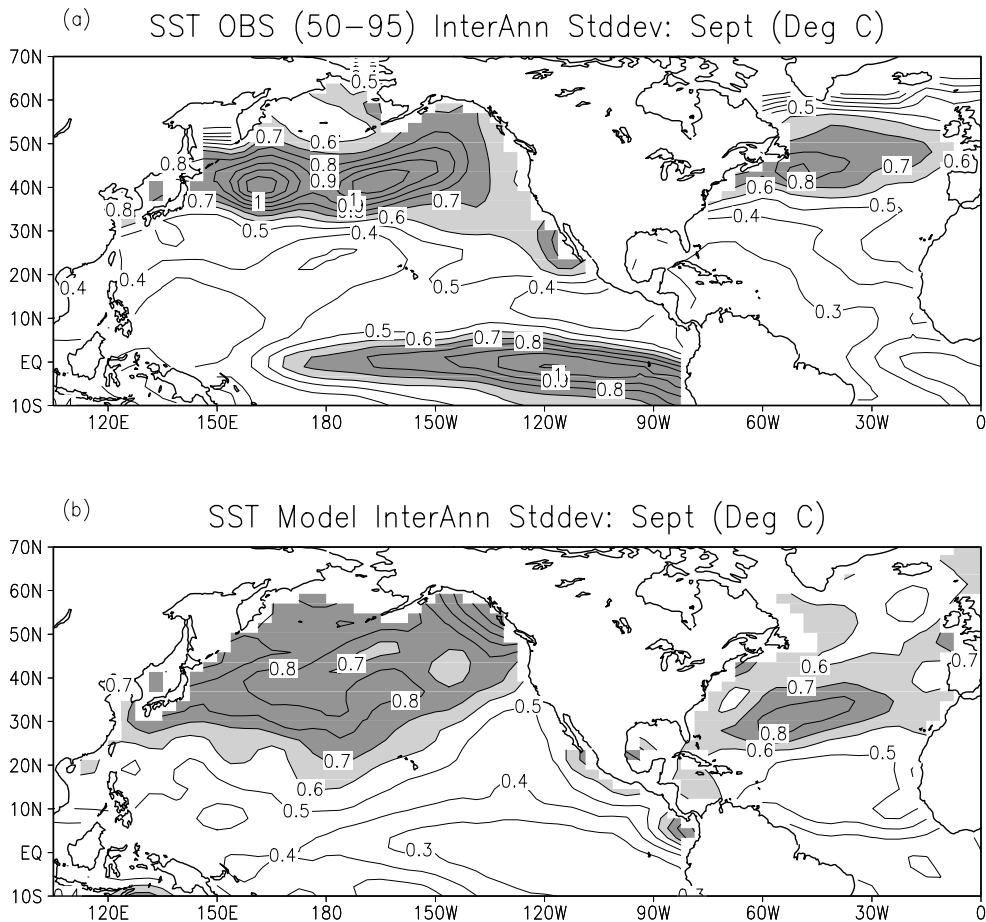


Fig. 3. The (a) observed and (b) simulated standard deviation of September SSTs ($^{\circ}\text{C}$). Contour interval and shading as in Fig. 2.

1995 and SSTs are provided by the MLM elsewhere over the global oceans. Including the observed ENSO signal generally improves the simulation of SST variability in the North Pacific, including a $\sim 15^\circ$ northward shift in the maximum SST σ to 30°N - 40°N in the central Pacific; a decrease in σ in the Sea of Japan; and a slight increase in σ in the northeast portion of the basin (not shown).

The SST σ from observations and the model simulation during September are shown in Figure 3. Both the observed and the simulated variability are greater in September than in March, primarily due to the relatively small thermal inertia of the shallow mixed layer in summer (see section 4). The observed SST σ in September exceeds 0.6°C over both oceans between 30°N - 50°N and reaches a maximum of 1°C along 40°N in the Pacific. The simulated σ also exceeds 0.6°C in both basins, but the region of enhanced variability is located about 15°

farther south in the Atlantic compared to observations. While the region of SST $\sigma > 0.6^\circ\text{C}$ is close to that observed in the North Pacific, it extends too far south in the central Pacific and does not cover the eastern Pacific from 20°N to 35°N . The model simulates regions where $\sigma > 0.7^\circ\text{C}$ in the North Pacific but it is too broad compared to observations.

Studies by *Norris and Leovy* [1994] and *Norris et al.* [1998] indicate that variability in stratus clouds contributes to SST anomalies in the central North Pacific during summer. As discussed in section 2, the GFDL model like most AGCMs have difficulty simulating clouds, especially low-level stratus decks. Thus some of the differences between the observed and simulated SST σ in September may result from errors in the simulated stratus clouds and the attendant surface shortwave radiation.

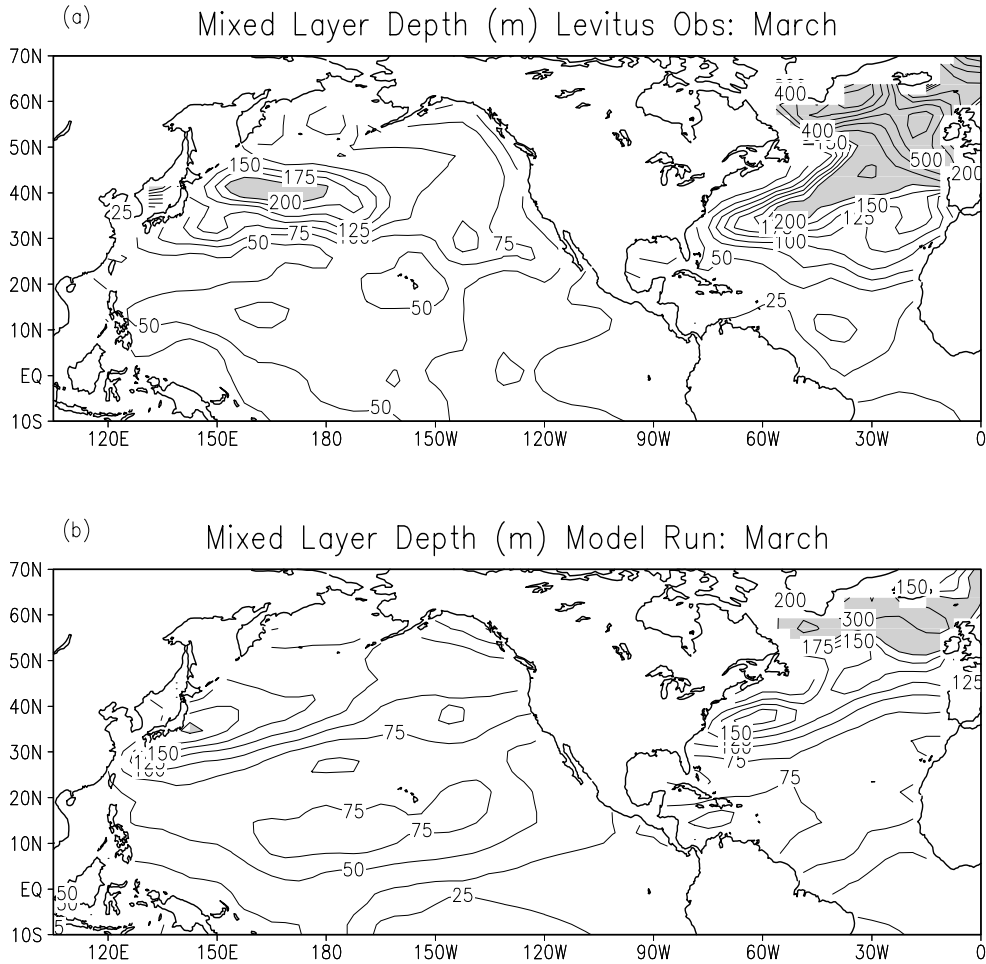


Fig. 4. The (a) observed and (b) simulated mixed layer depth (m) in March. The observed h values are from Monterey and Levitus (1997) which have then been interpolated from a $1^\circ \times 1^\circ$ grid to the R30 grid. Note that the contour interval changes: it is 25 for $h < 200$ and 100 for $h > 200$; values greater than 200 are shaded.

As expected, the model strongly underestimates the SST variability associated with ENSO in the tropical Pacific during September. Unlike March, there is no clear change in the pattern or strength of the variability outside of the tropical Pacific in the model simulation which included the specified ENSO signal. This is consistent with *Horel and Wallace* [1981], *Mitchell and Wallace* [1996], and *Kumar and Hoerling* [1998], who found that the extratropical atmospheric changes associated with ENSO are much greater in winter than in summer.

The observed and the simulated mean mixed layer depth (h) are shown in Figure 4 for March. The observed h is obtained from *Monterey and Levitus* [1997] based on the depth where the density is 0.0125 kg m^{-3} less than the surface density. The observed h values, which were originally on a $1^\circ \times 1^\circ$ grid, have been interpolated onto to the models Gaussian grid.

The observed mixed layer reaches its greatest depth in the North Atlantic where it exceeds 500 m from the Labrador Sea to east of Scotland. In nature, the formation of deep water through complex convective processes can lead to instantaneous mixed layer values of greater than 1500 m in the Labrador and Greenland Seas [*Gascard and Clarke*, 1983; *Dickson et al.*, 1996]. A secondary maximum in the observed h extends northeastward across the central Atlantic. The MLM simulates the observed structure of h but underestimates its magnitude especially north of $\sim 45^\circ\text{N}$.

The observed March mixed layer depths are much smaller in the Pacific where there is no deep water formation. The observed h reaches a maximum value of ~ 200 m, slightly greater than h in the coupled model integration. The observed and simulated h maxima are located in the western Pacific between 30°N and 45°N , but the center of this maximum is located 5° to the south and closer to the coast in the model. The elongated regions of enhanced h between 30°N and 50°N in both oceans are coincident with the surface forcing associated with the main storm tracks [*Alexander and Scott*, 1997]. Unlike observations, the model does not contain a narrow region of shallow h along the west coast of North America perhaps due to the absence of coastal upwelling in the MLM. The observed and simulated h range between 25 and 75 m throughout the tropics.

Several factors may contribute to the underestimation of h during winter in the coupled model simulation: (1) The MLM tends to shoal too rapidly under stable conditions and thus may be unable to maintain deep mixed layers through late winter. (2) Many ocean processes that generate turbulence are not included in the MLM, such as surface wave breaking, Langmuir cells, inertial current shears. (3) The surface mechanical forc-

ing is proportional to the cube of the wind speed, and the buoyancy forcing depends on the square of the wind speed; thus h deepens significantly during short periods of high wind speed. The surface boundary conditions are averaged over one day, which suppresses extreme short-duration forcing. (4) The mixed layer is constrained to be less than 850 m in the MLM, thereby limiting h when deep convection occurs. (5) The MLM does not include currents, which limits h due to the absence of mixing due to vertical shear and the advection of heat and salt which can change the vertical stability of the water column. Both of these processes are likely to be important in the western boundary currents and the subpolar gyre of the North Atlantic, where the MLM greatly underestimates h . (6) The observed mixed layer depth is estimated from the mean temperature and salinity profiles, while in the MLM, h is the layer over which surface-generated turbulence is active.

The observed and simulated mixed layer depths are at a minimum in June-August (not shown) but are still quite shallow in September (Figure 5). The model closely approximates observations with h of the order of 20 m in the central North Atlantic and much of the North Pacific, and somewhat deeper mixed layers north of 50°N in the Atlantic and in the subtropics of both ocean basins. The MLM also reproduces the observed minimum in h between 0° and 10°N and the deepening of the mixed layer from 0° to 10°S .

Basin-wide estimates of the interannual standard deviation of mixed layer depth are not available from observations; the simulated σ of h are shown in Fig. 6 for March and September. The regions of greatest variability coincide with the maximum mean h values both in winter and in summer (cf. Figures 4 and 5). The σ of h is greatest in the North Atlantic in March where it exceeds 30 m north of $\sim 30^\circ\text{N}$ and 60 m from about 45°N to 65°N . While h σ in March exceeds 30 m over much of the northwest Pacific and in the vicinity of Hawaii, it is less than 60 m over the entire Pacific. The variability is greatly reduced in September when the σ of $h < 5$ m over much of the ocean between 30°N and 60°N and has a maximum of 15-20 m at 15°N and 10°S in the central Pacific and western Atlantic.

4. Components of the SST tendency equation

The factors which control the SST tendency in the MLM, shown on the right-hand side of equation (1), are associated with fluxes through the surface and the base of the mixed layer. Multiplying eq. (1) by $\rho c h$ gives the terms in flux form: the net surface heat flux (Q_{net}); surface flux correction (Q_{cor}); penetrating solar radiation (Q_{sw}), entrainment heat flux ($Q_{we} = \rho c W_e \Delta T$); convec-

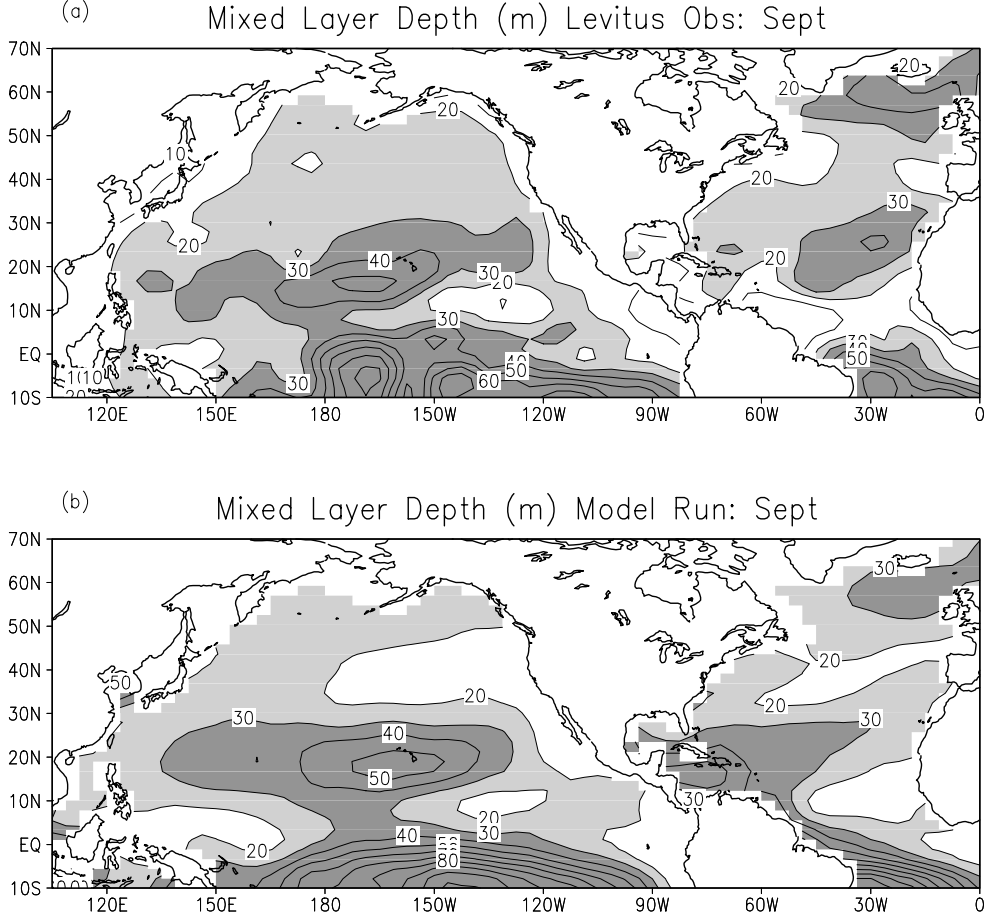


Fig. 5. The (a) observed and (b) simulated mixed layer depth (m) in September. The contour interval is 10, where $20 < h < 30$ is shaded light and $h > 30$ is shaded dark

tive adjustment (CA); and temperature diffusion at h (T_{dif}). The seasonal cycle of the zonal average of these six terms, obtained from the long term monthly means of the simulated fluxes, are shown in Figure 7.

As expected, Q_{net} is the dominant term over much of the Northern Hemisphere, with magnitudes exceeding 80 W m^{-2} north of 20°N in summer and winter. Heating due to solar radiation in summer and cooling by the sensible and latent heat fluxes in winter results in a strong seasonal cycle of Q_{net} with a maximum amplitude of 200 W m^{-2} at $\sim 40^\circ\text{N}$. However, the total flux through the surface is reduced by Q_{cor} which is roughly half as large as Q_{net} but of opposite sign. Q_{we} acts to cool SSTs over most of the Northern Hemisphere, since W_e is always positive and $\Delta T (=T_b - T_m)$ is negative over most of the world oceans. When $|\Delta T|$ reaches a maximum in fall, Q_{we} is similar in magnitude to Q_{net} , exceeding $|80| \text{ W m}^{-2}$ between 35°N and 60°N . The other three components, CA , Q_{sw} , and T_{dif} , are substan-

tially smaller (note that the contour interval is one fourth as large compared with the other three components) over most of the globe. CA is negligible except at high latitudes in winter when episodic deep convection brings warm salty water into the mixed layer. Q_{sw} cools the mixed layer, primarily in the subtropics in summer when the surface solar radiation is a maximum and h is a minimum. Like entrainment, T_{dif} acts to cool the mixed layer primarily at midlatitudes in fall when $|\Delta T|$ is a maximum.

The σ values for Q_{net} and $Q_{we} + CA$ over the course of the seasonal cycle, shown in Fig. 8, are computed from the departure of monthly means from the 50-year mean at each model grid point which are then zonally averaged. Recall that the seasonal cycle of the flux correction is the same each year ($Q_{cor} \sigma = 0$). W_e have combined CA with Q_{we} since the former represents convective plumes, an extreme form of entrainment. The $Q_{net} \sigma$ has a maximum in winter opposite to the mean Q_{net} . However, the simulated variability of Q_{net} may be

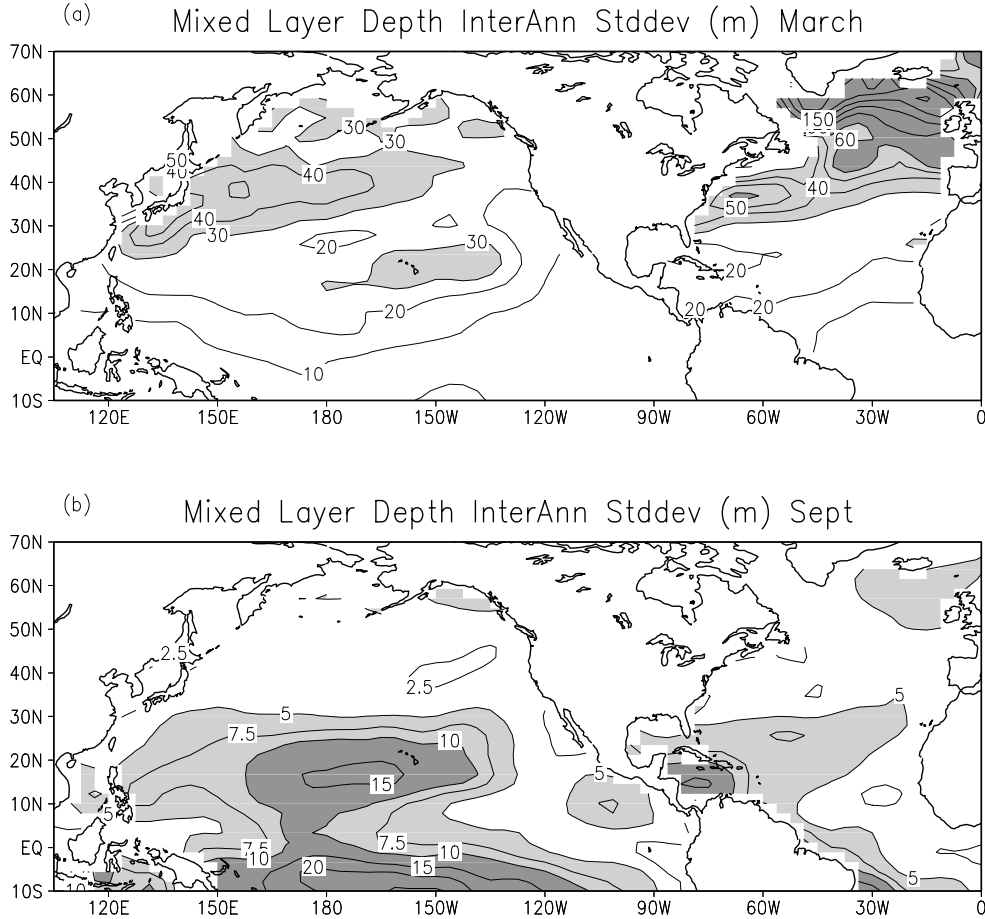


Fig 6. The simulated standard deviation of mixed layer depth (m) in (a) March and (b) September. In (a) values of $h\sigma < 30$ m have a contour interval of 10 and are shaded light, while $h\sigma > 30$ m have a contour interval of 30 and are shaded dark. The contour interval in (b) is 2.5 where $5 < h\sigma < 10$ is shaded light and $h\sigma > 10$ is shaded dark.

underestimated due to the lack of low cloud variability. The seasonal cycle of the σ of Q_{net} tends to lag the mean by about one month; for example the magnitude of the mean (σ) Q_{net} is maximized in January (February). The $Q_{we}+CA$ σ has two maxima exceeding 25 W m^{-2} , one at high latitudes in winter and the second in midlatitudes in fall; the former (latter) is due to variability in CA (Q_{we}). The general zonal structure of the σ of Q_{sw} and T_{dif} resemble their means, with maximum values of 8 and 4 W m^{-2} , respectively (not shown).

The spatial structure of Q_{net} in the R30 version of the GFDL is in general agreement with observations [Alexander and Scott, 1997]. The mean $Q_{we}+CA$ from the coupled model simulation in March and September is shown in Figure 9. During March, $Q_{we}+CA$ is relatively weak over both ocean basins with the strongest cooling ($< -30 \text{ W m}^{-2}$), south of Japan, at 10°N in the central Pacific, and at 50°N in the central Atlantic. CA

leads to warming ($> 30 \text{ W m}^{-2}$) south of Greenland (not shown). In September, when CA is negligible, Q_{we} is fairly zonal in structure and decreases poleward. The maximum cooling occurs in the northwestern Pacific, where the magnitude of Q_{we} exceeds 100 W m^{-2} , roughly twice that in the Atlantic at the same latitude. $Q_{we}+CA$ weakly warms the tropical Pacific as $\Delta T > 0$. In this region, $P-E > 0$ increases the surface buoyancy creating a shallow mixed layer (Figures 4 & 5) that is often maintained by a jump in salinity. Observational studies by Lukas and Lindstrom [1991] and Anderson *et al.* [1996] also indicate that entrainment acts to slightly warm the mixed layer and helps to maintain high SSTs in the tropical West Pacific. The warming due to $Q_{we}+CA$ in the eastern equatorial Pacific during September in the model is unrealistic.

Previous studies [e.g., Cayan, 1992; Iwasaka and Wallace, 1995; Delworth, 1996; Deser and Timlin, 1997] along with Figure 8 indicate that variability in

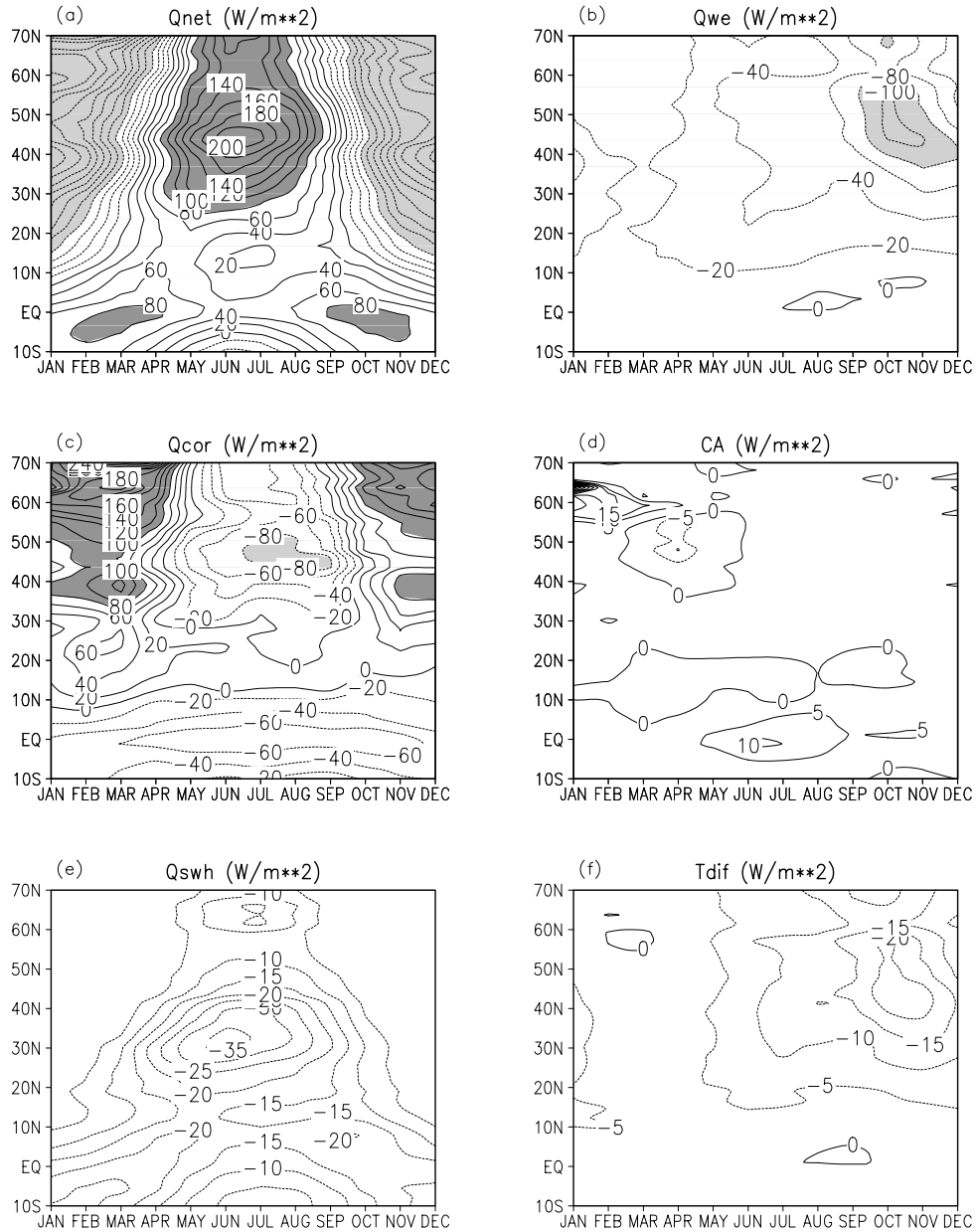


Fig. 7. Zoally averaged (a) net surface heat flux, (b) entrainment heat flux, (c) surface heat flux correction, (d) convective adjustment (e) penetrating solar radiation, and (f) temperature diffusion (Wm^{-2}) in the MLM as a function of calendar month. The contour interval is 20 in (a)-(c) and 5 in (d)-(f). Negative contours are dashed and values <-80 (>80) are shaded light (dark).

Q_{net} plays an important role in the development of SST anomalies. Here we assess the relative importance of entrainment in generating SST variability by taking the ratio of $(Q_{we}+CA)\sigma$ to $Q_{net}\sigma$ during March and September (Figure 10). During March $(Q_{we}+CA)\sigma/Q_{net}\sigma$ is small, between 0.2 and 0.4, over most of the ocean north of 10°S , except for the tropical West Pacific and in the Atlantic north of 30°N . Ratios that exceed unity in the North Atlantic are due to CA rather than Q_{we} . The

$(Q_{we}+CA)\sigma$ also exceeds that of $Q_{net}\sigma$ in the vicinity of the equator near 160°E , which may be related to interannual variability in the strength of the Madden-Julian Oscillation [Shinoda and Hendon, 1998].

Variability in the entrainment heat flux clearly plays an important role in generating SST anomalies during September over much of the Atlantic (Pacific) north of 45°N (35°N) where $(Q_{we}+CA)\sigma/Q_{net}\sigma > 1.0$. During summer, most of the heat flux across the base of

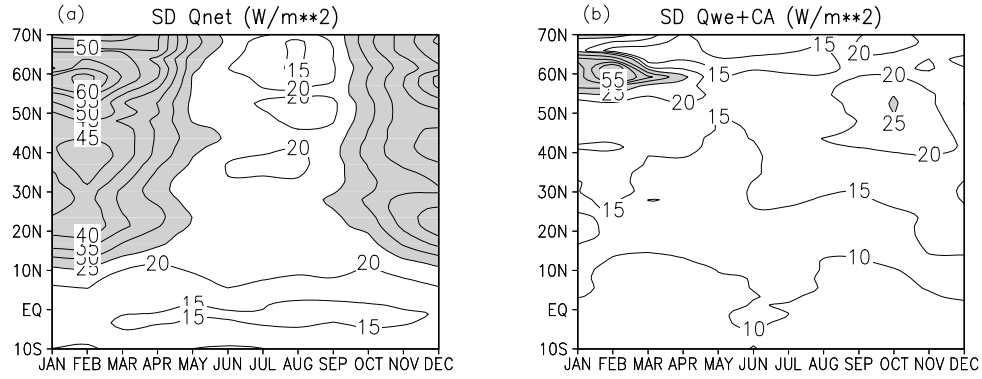


Fig. 8. Zonally averaged standard deviations of (a) the net surface heat flux and (b) the heat flux due to entrainment plus convective adjustment (Wm^{-2}) as a function of calendar month. Q_{net} and $Q_{we} + CA \sigma$ are computed using monthly anomalies at each MLM grid point and then zonally averaged. The contour interval is 5, values greater than 25 are shaded.

the mixed layer is associated with mixing in a convectively stable environment, and thus $Q_{we} \sigma \gg CA \sigma$.

The development of the simulated SST anomalies,

due to surface heat fluxes and entrainment, the dominant processes in the MLM, is examined further by decomposing the variables in eq. 1 into daily mean ($\bar{\quad}$) and

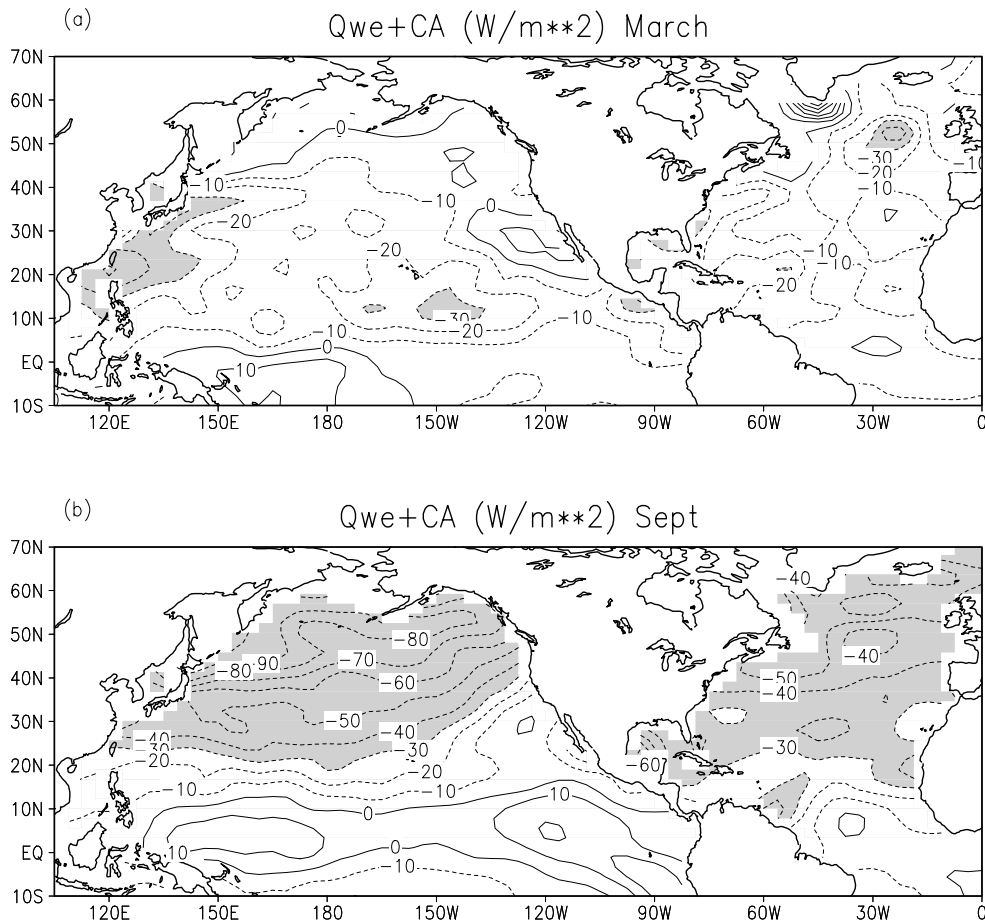


Fig. 9. The heat flux due to entrainment plus convective adjustment (Wm^{-2}) in (a) March and (b) September. The contour interval is 10, values less than 30 are shaded.

departures (') from the mean. Clark [1972] and Alexander and Penland [1996] have performed a similar analysis, using the approximation $1/(\bar{h}+h') \approx 1-(h'/\bar{h})$, which is valid only when $h'/\bar{h} < 1$, a condition that is violated over parts of the ocean especially in spring and summer. Here $h \equiv 1/\eta$, then using eq. (1) the anomalous T_m tendency can be written as :

$$\frac{\partial T'_m}{\partial t} = \frac{Q'_{net}\bar{\eta}}{\rho c} + \frac{(\overline{Q_{net}} + \overline{Q_{cor}})\eta'}{\rho c} + \frac{Q'_{net}\eta' - \overline{Q'_{net}\eta'}}{\rho c}$$

$$+ \frac{W'_e\overline{\Delta T\eta}}{\rho c} + \frac{\overline{W_e\Delta T\eta'}}{\rho c} + \frac{\overline{W_e\Delta T\eta'}}{\rho c}$$

$$+ (W'_e\Delta T' - \overline{W'_e\Delta T'})\bar{\eta} + (W'_e\eta' - \overline{W'_e\eta'})\Delta T'$$

$$+ (\Delta T'\eta' - \overline{\Delta T'\eta'})\overline{W_e} + W'_e\Delta T'\eta' - \overline{W'_e\Delta T'\eta'} + CA'. \quad (3)$$

Composites of the individual terms in (3) are constructed at each model grid point based on when the local monthly value of $\frac{\partial T'_m}{\partial t} > 1\sigma$. Composites are computed for each calendar month by summing daily values of each term during the months when the σ criterion is exceeded. Approximately 10 months of data went into each composite.

Analyses of zonal means of the terms in eq. (3) indicates that only the first six make a significant contribution to T_m anomaly development and that the contribution of the individual terms is distinctly different in the tropics and midlatitudes but relatively uniform north of $\sim 20^\circ\text{N}$ (not shown). Figure 11 shows the seasonal cycle of the first six terms on the right-hand side of (3) averaged between 20°N and 70°N . Term I is dominant throughout the year, indicating that Q'_{net} strongly contributes to the fastest growing SST anomalies. Even

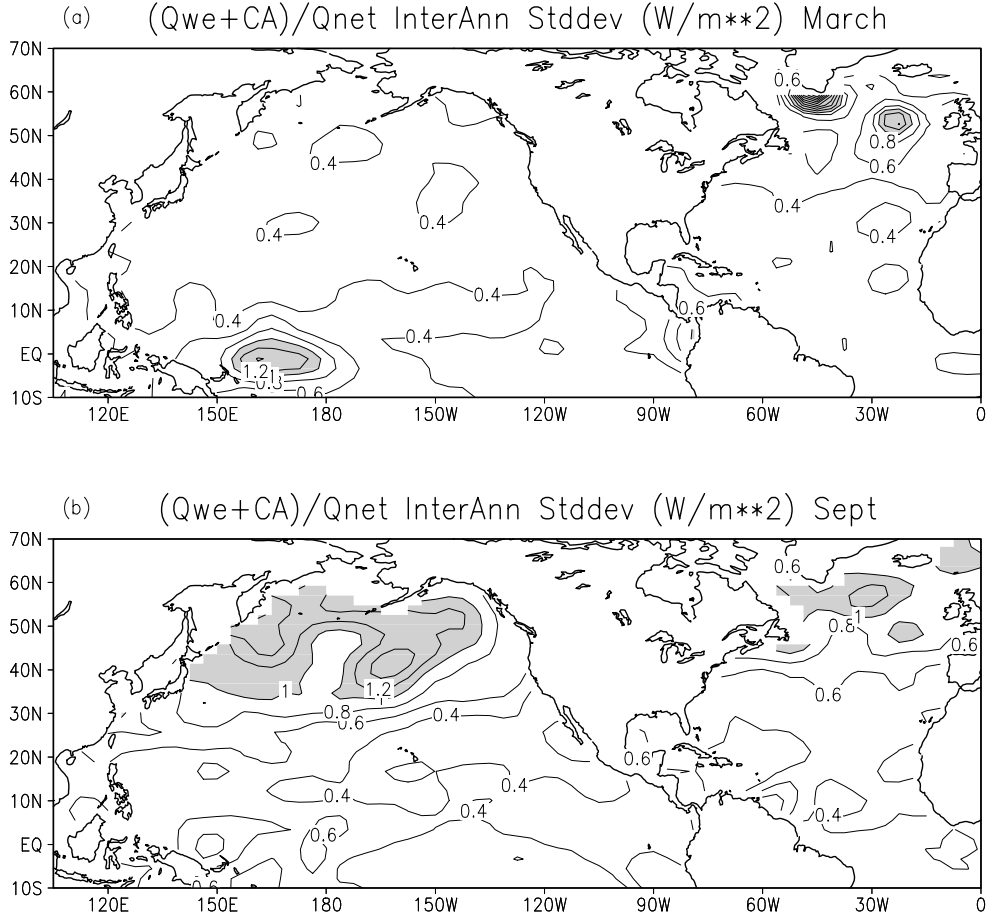


Fig 10. The standard deviation of entrainment heat flux plus convective adjustment divided by the standard deviation of the net surface heat flux $(Q_{we}+CA)\sigma/Q_{net}\sigma$ in (a) March and (b) September. The contour interval is 0.2, values greater than 1.0 are shaded.

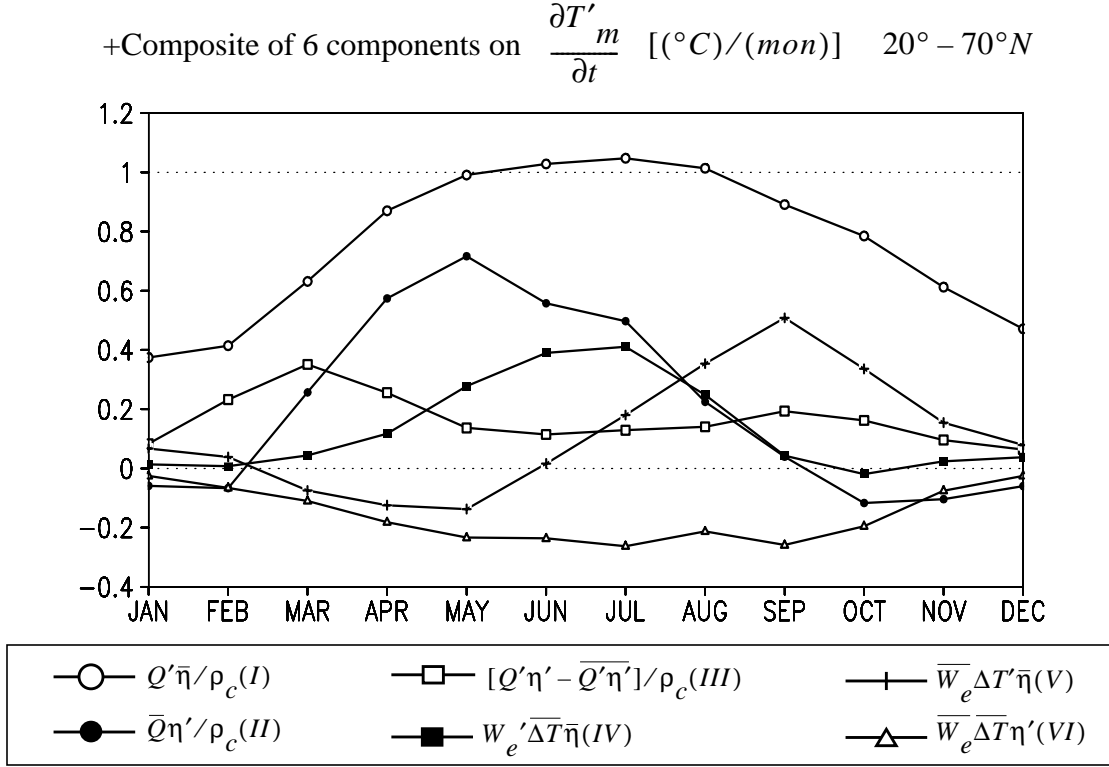


Fig. 11. Composite of the six leading components ($^\circ\text{C mon}^{-1}$) of the SST tendency equation (3) as a function of calendar month. The composites are constructed at each MLM grid point based on when the local monthly SST tendency exceeds one standard deviation, the resulting values are then averaged between 20°N - 70°N .

though Q'_{net} is 2-3 times larger in winter than in summer (Figure 8), $\eta (=1/\bar{h})$ is an order of magnitude smaller in winter than summer (Figures 4 & 5), as a result term I ranges from about $0.4^\circ\text{C month}^{-1}$ in January to $1.0^\circ\text{C month}^{-1}$ in July. Term II plays an important role in generating SST during spring and summer, in general agreement with Clark [1972] and Alexander and Penland [1996], although they estimated its impact to equal or exceed term I. Term III depends on how the instantaneous relationship between Q_{net} and η differs from their long-term correlation. The net surface heating causes a more buoyant and thus shallower mixed layer, which results in a positive correlation between Q'_{net} and η' . During early spring the distribution of η' is highly skewed, since the mixed layer tends to shoal abruptly but only gets marginally deeper than the mean. As a result, $Q'_{net}\eta' > \bar{Q}'_{net}\bar{\eta}'$ and thus term III makes a significant contribution in February-April to the positive $\frac{\partial T'_m}{\partial t}$ composite, but is negligible for the negative composite (not shown). Term IV, associated with the anomalous entrainment rate, is maximized in July when it

contributes $\sim 0.4^\circ\text{C month}^{-1}$ to SST anomaly growth. Positive values of term IV result from weaker entrainment of colder water from below ($W'_e < 0$), since $\bar{\Delta T} = \bar{T}_b - \bar{T}_m < 0$ and $\bar{\eta} > 0$. Term V, which represents the mean entrainment of the anomalous temperature jump at the base of the mixed layer, reaches a maximum in September, when $\Delta T'$ and $\bar{\eta}$ are large. Term VI always acts to damp SST anomaly growth, as \bar{W}_e is positive, $\bar{\Delta T}$ is almost always negative, and the mixed layer tends to be shallower ($\eta' > 0$) when it is warming rapidly.

5. Winter-to-Winter SST Autocorrelation

In the previous section we examined how variations in mixed layer depth influenced SST anomaly development; here we explore how the seasonal cycle of h , which is very large over the North Atlantic (see Figures 4 & 5), can affect the persistence of SST anomalies. The local winter-to-winter SST autocorrelation at each grid point over the North Atlantic from observations and the model are shown in the left panels of Figure 12.

Winter-to-Winter SST Autocorrelation

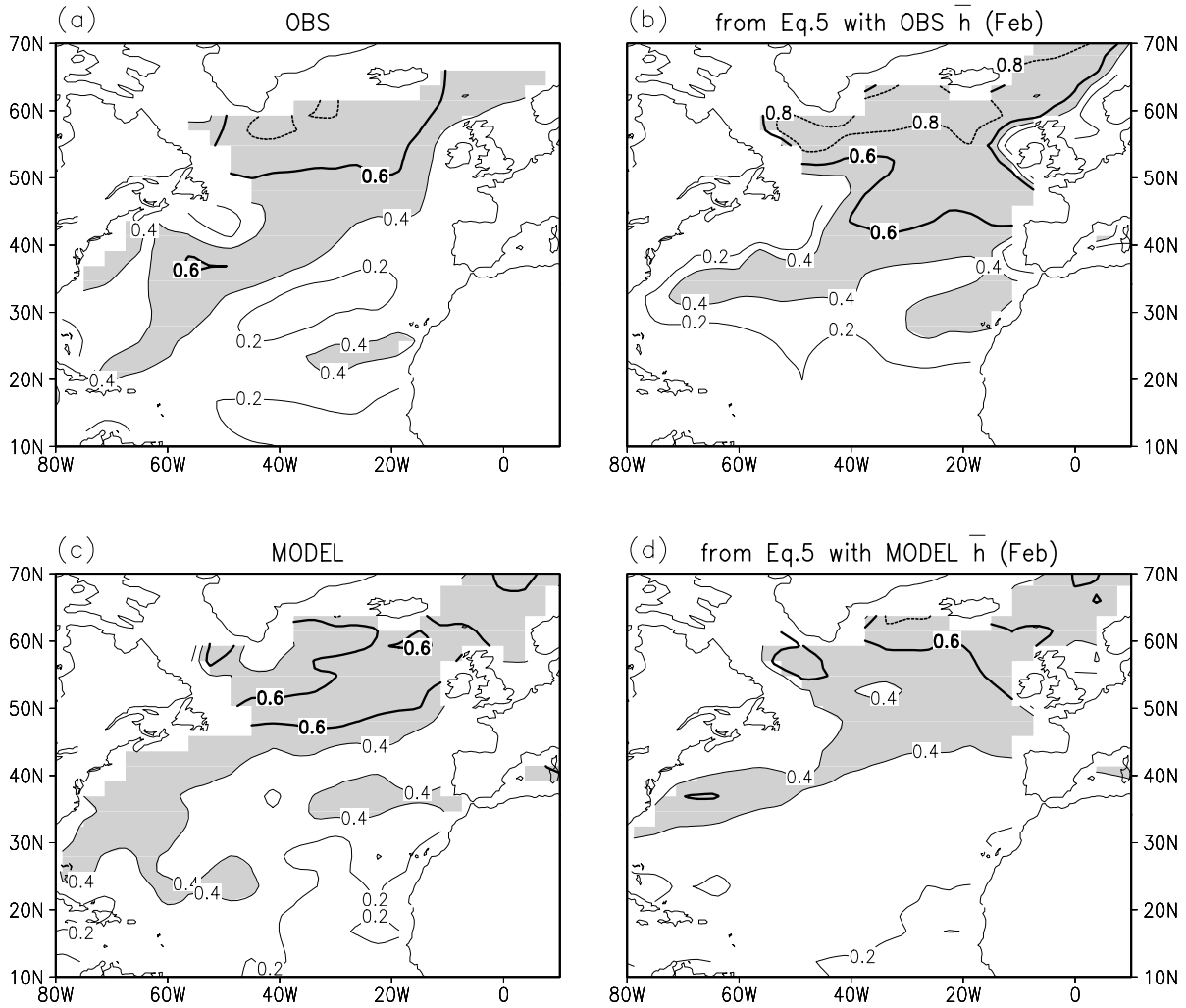


Fig. 12. Local correlations of SST anomalies from one winter (January-March) to the next over the North Atlantic. Left panels are from (a) observations [Smith et al. 1996] for the period 1948-1997 and (c) the MLM, right panels are computed from Eq. 5 with $l = 17.5 \text{ Wm}^{-2} \text{ }^{\circ}\text{C}$ and \bar{h} in February from (b) observations [Monterey and Levitus 1997] and (d) the MLM. Values greater than 0.4 are shaded, the 0.6 (0.8) contour is bold (dashed).

Winter is defined as January-March when mixed layer depths reach their climatological maximum. The observed and simulated autocorrelation patterns are similar, with highest values (0.6 to 0.8) north of about 50°N in the region of deepest winter mixed layers and lowest values (0.2 to 0.4) in the eastern subtropics where h is relatively small. The observed autocorrelations between Greenland and Iceland are somewhat higher than those in the MLM, a region where the model also underestimates h during winter.

A stochastic framework for climate variability, first proposed by Hasselmann [1976], is helpful for under-

standing the SST autocorrelation pattern. Frankignoul and Hasselmann [1977] showed that in the simplest stochastic model for midlatitude SST anomalies:

$$(\rho ch) \Delta SST' / \Delta \tau = -\lambda SST' + F'; \quad (4)$$

where F' represents white-noise atmospheric forcing. The linear damping parameter l is a highly simplified representation of the thermodynamic and dynamic feedback of an SST anomaly upon the net surface heat flux at the sea surface: typical values are estimated to be in the range $15\text{-}20 \text{ Wm}^{-2} \text{ }^{\circ}\text{C}^{-1}$ [Barsugli and Battisti, 1997; Seager et al., 1995; Saravanan, 1998; Franki-

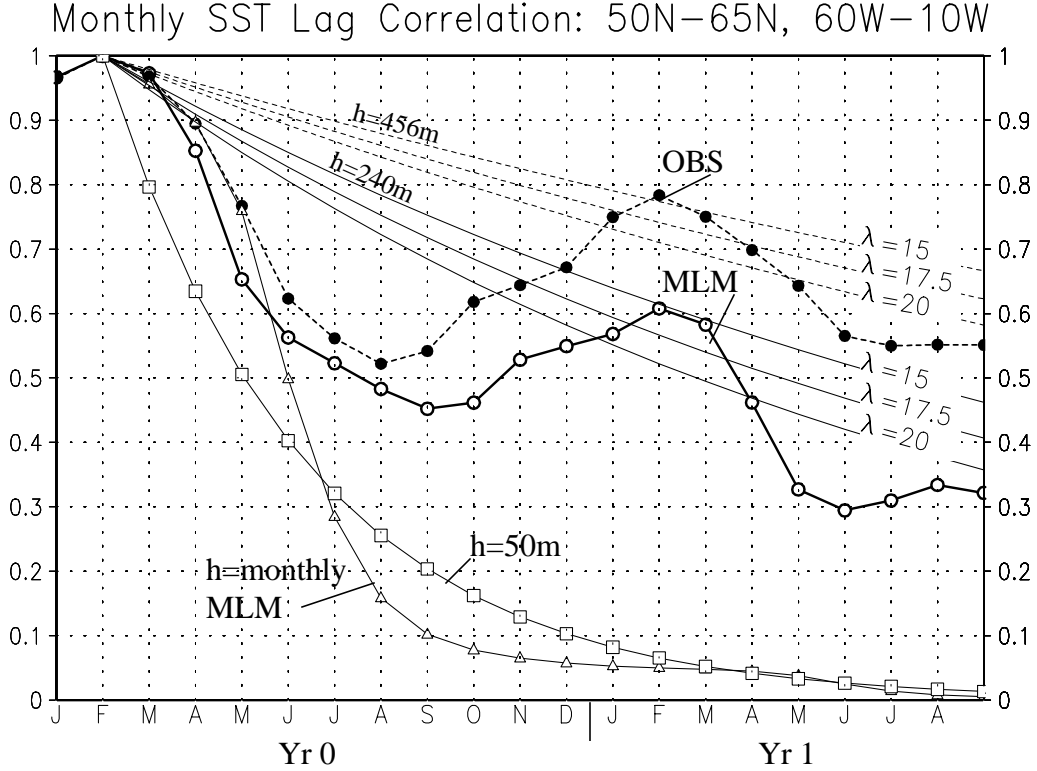


Fig. 13. Correlation of February SST anomalies with monthly SST anomalies from the previous January through the following September for a region in the far North Atlantic (50°N-65°N, 60°W-10°W). Values are plotted for the observations (solid circles) and the MLM (open circles). The other curves are computed using Eq. 5: with $l = 15, 17.5,$ and $20 \text{ Wm}^{-2} \text{ } ^\circ\text{C}^{-1}$ and \bar{h} in February from observations (456 m; dashed line) and from the MLM (240 m; solid line); with $l=17.5$ and $h=50 \text{ m}$ (squares); and with $l=17.5$ and monthly values of \bar{h} averaged over the domain from the MLM (triangles).

gnoul et al., 1998]. If h is treated as a constant, the SST autocorrelation function at lag τ takes the simple form:

$$R(\tau) = \text{Exp} -l/(\rho c h) \Delta\tau. \quad (5)$$

The one-year lag SST autocorrelations $R(1\text{yr})$ over the Atlantic calculated from eq. (5) with λ set to $17.5 \text{ Wm}^{-2} \text{ } ^\circ\text{C}^{-1}$ and h obtained from observations and the MLM are shown in Figure 12 (right-hand panels). The $R(1\text{yr})$ values were derived using \bar{h} in February; nearly identical results are obtained when using March \bar{h} values (not shown). The distribution of autocorrelations computed from eq. (5) broadly resembles the observed autocorrelations (top panels) and those from the coupled model (bottom panels). The spatial correlation coefficient between the top (bottom) panels over the North Atlantic (10°N-65°N, 65°W-0°W) is 0.65 (0.67).

The monthly lag autocorrelations of SST anomalies averaged over the region of deep winter mixed layers in the far North Atlantic (50°N-65°N, 60°W-10°W) are shown in Figure 13. The observed and the simulated

values are obtained by correlating the SST anomalies in February with those in the previous January through the following June. The autocorrelations in both the model and observations exhibit a steep decline during spring (April-June), attain a minimum in summer (July-September), and reach a secondary maximum the following winter (January-March). The shape of the autocorrelation function is characteristic of the "reemergence" mechanism discussed by Namias and Born [1970, 1974] and Alexander and Deser [1995], in which atmospherically-forced thermal anomalies in the deep winter mixed layer, become sequestered beneath a shallow summer mixed layer, and are then reentrained into the mixed layer the following fall and winter.

Autocorrelation functions for SST' computed using eq. (5) with different values for l and h are also shown in Figure 13. Autocorrelation functions computed with l set to 15, 17.5, and $20 \text{ Wm}^{-2} \text{ } ^\circ\text{C}^{-1}$ and where \bar{h} is obtained from either observations or the MLM averaged over the region during February, indicate that the observed and simulated winter-to-winter

SST' correlations can be explained by the stochastic climate model, provided that h is given by its winter value. Autocorrelation functions calculated with both h set to 50 m, the depth often chosen for slab models, and with a more realistic seasonally-varying h , indicate that a slab mixed layer *without entrainment* predicts an erroneously rapid decay of wintertime SST anomalies.

Why does the simple formula for $R(1)$ in eq. (5) work reasonably well when h is set to its winter value, given that h is an order of magnitude smaller in summer than in winter? Because of the storage of thermal anomalies created during winter in and below the summer seasonal thermocline, the effective h can be approximated by its maximum value when considering winter-to-winter relationships. Since the negative air-sea feedback is confined to the shallow surface layer in summer, there is little damping of the thermal anomalies in the seasonal thermocline (this was confirmed by the persistence of the heat content anomalies extending from 30 m to the h maximum at several locations in the North Atlantic in the MLM.) Thus, the value of l used in eq. (5) represents an average damping rate over the entire year, with more (less) damping of the temperature anomalies over the effective h in winter (summer). Many additional factors influence l , including the mean wind speed, depth of the atmospheric boundary layer and proximity to land, while oceanic processes such as subduction and horizontal and vertical diffusion also act to damp SST anomalies. A detailed stochastic model, with damping parameters that depend on location is beyond the scope of this paper, although such models have been developed by *Frankignoul and Reynolds*

[1983], *Herterich and Hasselmann* [1987], *Frankignoul et al.* [1998], and *Ostrovskii and Piterbarg* [1985].

6. Components of the Entrainment Equation

The entrainment rate in the MLM, given by eq. (2), is governed by u_*^3 , $B(h)$, and Δb which represent wind stirring, buoyancy forcing integrated over the mixed layer, and the buoyancy jump at the base of the mixed layer, respectively. Correlations between these three terms and W_e are computed for each calendar month using daily anomalies of u_*^3 , $-B(h)$, and $-\Delta b$ only on days when entrainment has occurred. Negative values of $B(h)$ and Δb anomalies should enhance entrainment all other factors being equal. Averages of the correlations for all of the ocean model grid points between 20°N and 70°N are shown in Figure 14. The correlation between W_e and u_*^3 anomalies ranges between about 0.35 in February to 0.6 in June. In contrast, the correlations between W_e and $-B(h)$ peak near ~ 0.6 in winter and decrease to ~ 0.3 in summer. Correlations between W_e and $-\Delta b$, while generally small, approach ~ 0.3 in fall.

The analysis above examines the linear relationship between W_e and the anomalous forcing terms. In some mixed layer models, including the one described by *Niiler and Krauss* [1977], dissipation is a constant fraction of the individual forcing terms, so their contribution to W_e can be determined independently [*Hanson, 1992*]. In the MLM dissipation is non-linear: ϵ in eq. (2)

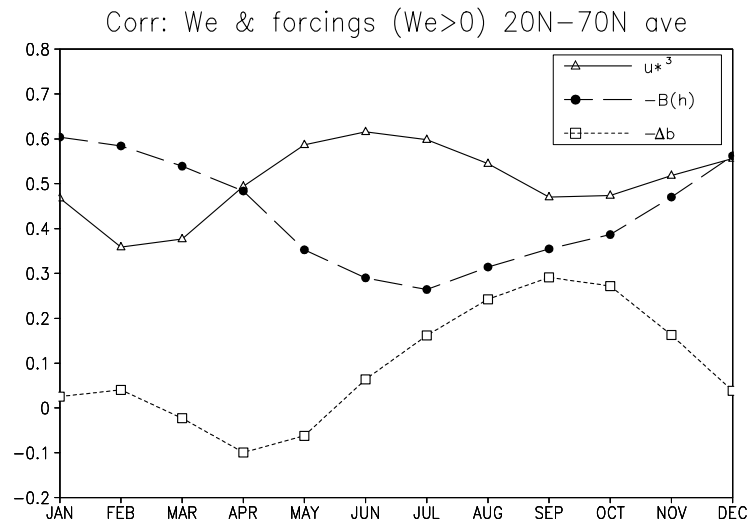


Fig. 14. Correlations of the entrainment rate (W_e) with the friction velocity (u_*^3), and the negative buoyancy forcing integrated over the mixed layer ($-B(h)$), and buoyancy jump at the base of the mixed layer ($-\Delta b$) computed using daily anomalies within a given calendar month.

is a complex function of $B(h)$, u_*^3 and u_*/f , where f is the Coriolis parameter. However, a nondimensional mixing efficiency can be defined:

$$P^* = h\Delta bW_e/u_*^3 \quad (6)$$

which is solely a function of h/L and h/λ [Gaspar, 1988], where $L(=u_*^3/B(h))$ is a bulk Monin-Obukhov length scale and $\lambda(=u_*/f)$ is the Ekman or Rossby rotation scale. Contoured values of $P^*(h/L, h/\lambda)$ are shown in Fig. 15. P^* increases as h/L decreases since more surface cooling ($B(h) < 0$) leads to enhanced mixing. P^* decreases as h/λ increases since rotation limits the vertical size of eddies. However, h/λ has a negligible impact on P^* for values of $h/L < \sim 5$.

A scatter plot of 50 years of monthly mean values of h/L versus h/λ averaged between 20°N - 70°N obtained from the coupled model simulation are also shown in

Figure 15. From September to April the seasonal cycle dominates the interannual variability, as all 50 values within a given month reside in a distinct area of the $h/L, h/\lambda$ phase space. The spread in the individual monthly values of h/L and thus P^* is largest in January and February. The maximum values of h/L (h/λ) occur in December-February (January-March), while the minimum of both length scales occurs in June-July. Figure 15 suggests that entrainment occurs much more often than shoaling, since P^* is almost always greater than zero. While P^* appears to depend much more strongly on L than λ , at a given time and location variations in λ can influence entrainment, especially from March through September.

The mean seasonal cycle of h/L versus h/λ in Figure 15 displays a "hysteresis loop": with a different path through the $h/L, h/\lambda$ phase space in the first and second half of the year. The hysteresis loop results from lags in the seasonal cycle between $B(h)$, u_* , and h ; zonal aver-

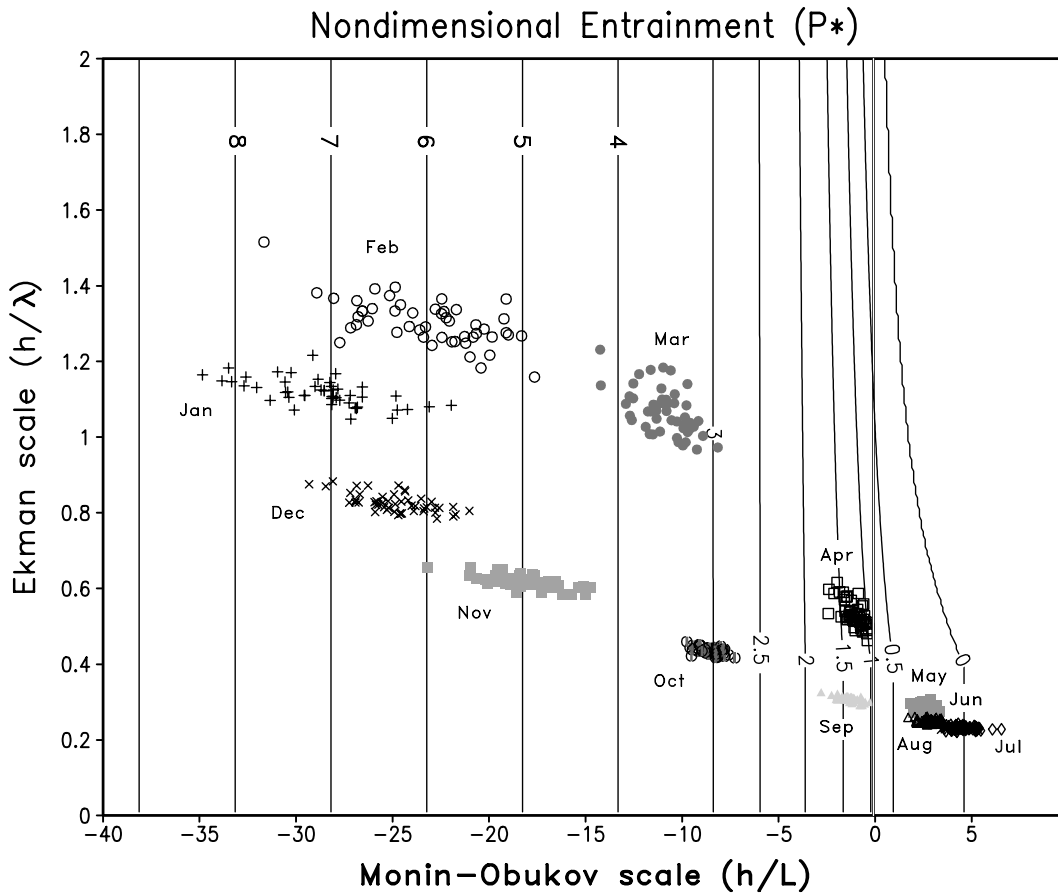


Fig 15. Non-dimensional mixing efficiency (P^*) as a function of the non-dimensional stability (h/L) and rotational (h/λ) parameters, which uniquely govern P^* in the MLM. The contour interval is 0.5 for $0.0 P^* < 3.0$ and 1.0 for $P^* > 3.0$. Overlaid on the P^* contours is a scatter plot of $h/L, h/\lambda$ obtained from the coupled model simulation, where h/L and h/λ are monthly means that have been averaged between 20°N - 70°N .

ages of the quantities reach a maximum in November, January, and March, respectively. Hysteresis loops in the seasonal cycles of heat content and SST or potential energy have been discussed by *Gill and Turner* [1976]. Figure 15 along with previous studies indicate that the hysteresis effect in the upper ocean depends on lags between the surface heating and mechanical forcing and on the physics of the mixed layer, which deepens by entrainment but shoals by reforming closer to the surface.

7. Summary

A coupled model consisting of an R30 atmospheric GCM connected to an ocean mixed layer model, is used to study variability of the upper ocean in the Northern Hemisphere. The ocean model consists of a grid of independent column models that allow for local air-sea energy exchange and the turbulent entrainment of water into the surface mixed layer, but exclude currents and vertical motion. With the application of a seasonally varying surface flux correction, the long term monthly mean SSTs in a 50-year integration of the coupled model remain close observations.

The model does a reasonable job of simulating SST variability in midlatitudes. Like observations, the interannual standard deviation (σ) of SST in the model is slightly higher in September than in March and varies between 0.4 and 1.2°C over most of the northern oceans in both months. However, the model is clearly deficient in the Gulf Stream region and the eastern tropical Pacific where currents and vertical motion strongly influence SSTs, and in the eastern portion of the subtropics where the AGCM does not properly simulate stratiform clouds. The model slightly underestimates SST σ , and the regions of maximum variability are located at about 20°N-30°N, 10°-15° south of their observed position. In an additional coupled model integration with observed SSTs specified in the tropical Pacific, the simulated SST σ maximum in the Pacific during March is located at ~35°N in agreement with observations, suggesting that SST variability in the central and eastern North Pacific during winter is dependent on ENSO.

The model simulates the general structure of the mean mixed layer depth (\bar{h}) north of 10°S in both March and September well, but underestimates its magnitude in the North Atlantic during winter. As discussed in section 3, there are many reasons why h might be too small in the subpolar gyre of the North Atlantic in winter; analyses of ocean GCMs could help to elucidate the influence of currents on vertical shear and stratification and thus h . The regions of greatest mixed layer depth variability coincide with the maximum (\bar{h}) in both winter and summer.

The surface and entrainment heat fluxes are the dominant terms in the SST tendency equation. The net surface heat flux strongly influences the mean seasonal cycle of SSTs and the development of SST anomalies throughout the year, but is especially dominant in winter. Entrainment of subsurface water into the mixed layer acts to cool SSTs over most of the Northern Hemisphere, except at high latitudes in the North Atlantic in winter and in portions of the tropical Pacific where the water is warmer at depth and salinity controls the density profile. Entrainment strongly influences SSTs anomalies in fall, especially north of ~35°N (45°N) in the Pacific (Atlantic). The impact of entrainment on SST' tendencies depends mainly on the anomalous entrainment ($W'_e \overline{\Delta T h}$) in summer and the anomalous temperature jump at the base of the mixed layer $\overline{W_e \Delta T' h}$ in fall. Anomalous entrainment also influences SSTs indirectly through the mixed layer depth, and h' has a significant impact on the SST' tendency during spring and summer. In agreement with *Alexander and Penland* [1996], the results of the present study suggest that while a fixed slab representation of the upper ocean may be reasonable in winter, changes in h and the heat flux through the base of the mixed layer play an important role in the development of SST anomalies during the remainder of the year. A slab mixed layer without entrainment and the storage of thermal anomalies beneath the mixed layer would predict an erroneously rapid decay of SST anomalies, both for a constant h or where h is specified to vary with the seasonal cycle. The ability of the MLM to simulate high (> 0.6) winter-to-winter SST anomaly correlations, in regions of deep winter mixed layers such as the far North Atlantic, suggests that mixed layer processes alone can lead to persistence of thermal anomalies: advection by ocean currents or the thermohaline circulation need not be invoked. These high autocorrelations can be explained using Hasselmann's stochastic climate model for SST anomalies under the assumption that the effective thermal capacity of the surface layer mainly depends on the wintertime h , not the annually averaged mixed layer depth.

Correlations between monthly anomalies of W_e and u_*^3 , $B(h)$ and Δb indicate that wind mixing is the dominant term driving anomalous entrainment in summer, buoyancy forcing is most important in winter, while the density jump at the base of the mixed layer is of secondary importance throughout the year. However, the mechanical and buoyancy forcings are linked through their mutual dependence on the wind speed. Entrainment in the mixed layer model used here is gov-

erned by the Monin-Obukhov ($u_*^3/B(h)$) and Rossby rotation (u_*/f) length scales. The former is dominant in the coupled model simulation especially in winter, although rotation can be important for determining whether shoaling occurs at any given time.

Our findings depend on several factors, including the a priori assumption of a mixed layer, the parameterizations used to estimate entrainment into the mixed layer, neglect of horizontal processes in the ocean model, the surface flux correction, Newtonian damping of temperature and salt anomalies, and the surface fluxes generated by the AGCM. Several studies that have compared the fidelity of one-dimensional ocean models have found that bulk models, including the one designed by *Gaspar* [1988], simulate conditions in the upper ocean as well as layered models [Martin 1985; Kraus 1988]. The flux corrections used here, are in general agreement with observed estimates of the ocean heat flux convergence, suggesting that the correction is primarily compensating for the absence of oceanic heat transport, rather than for errors in the atmosphere or ocean model. The correction and to a lesser degree the weak (10-year) Newtonian damping, keep the mean climate of the upper ocean close to the observed climate and thereby influence the simulation of mean quantities, such as the entrainment heat flux shown in Figure 9. However, it is crucial to have a reasonable ocean climate in order to examine the development of SST anomalies, as indicated by eq. (3). In addition, the correction has not been applied to the surface forcing when computing the entrainment rate, thus the correction only weakly influences h through its affect on the mean density profile.

More complex models, including coupled atmosphere-ocean GCMs, also have errors in their simulation of the mean climate state. Flux corrections have been applied in some coupled GCM simulations [Manabe and Stouffer 1988; Gordon and O'Farrell 1997], while others undergo climate drift and/or obtain reasonable SST estimates but from a heat balance that differs from observations [Moore and Gordon 1994; Bryan 1998; Kiehl 1998]. Since the mixed layer is mainly controlled by local processes, one-dimensional models can provide a useful means for testing parameterizations for vertical mixing in more complex ocean models.

In this paper we have focused on how surface fluxes and entrainment influences SST and mixed layer depth. Barsugli [1995] and Blade [1997] compared the behavior of a low-resolution atmospheric model coupled to a 50 m slab ocean to an atmospheric simulation with specified SSTs assuming perpetual January conditions. These studies along with the idealized modeling study of Barsugli and Battisti [1997] found that midlatitude air-sea coupling leads to a reduction in thermal damping

of air temperature anomalies by surface fluxes which results in an increase in the variance of the near surface air temperature and a slight enhancement of the persistence of certain atmospheric structures. Bhatt *et al.* [1998] confirmed the reduction of thermal damping in a coupled model which included the seasonal cycle and a variable depth mixed layer ocean model, but found that the subsurface storage of thermal anomalies and their re-entrainment into the mixed layer had an even greater impact on near surface air temperature variability on interannual timescales. In the future, we plan to compare the coupled model described here to an atmospheric GCM simulation in which the SSTs are specified to follow the long-term mean seasonal cycle of the coupled run to study how midlatitude air-sea interaction and mixed layer physics influence atmospheric variability.

Acknowledgements

We thank Gabriel Lau, Isaac Held, John Lanzante and Mary Jo Nath for providing to us the GFDL AGCM and model fields from the simulation with observed SSTs in the tropical Pacific as part of the GFDL-University Consortium project. Steve Worley at NCAR provided the observed mixed layer depth data. We also thank Joe Barsugli and Matt Newman for their valuable suggestions. This research was supported by NSF grant OCE95-31870 and NOAA grant GC98-139.

References

- Alexander, M.A., Midlatitude atmosphere-ocean interaction during El Niño. Part I: the North Pacific Ocean, *J. Climate*, **5**, 944-958., 1992.
- Alexander, M.A., and C. Deser, A mechanism for the recurrence of wintertime midlatitude SST anomalies, *J. Phys. Oceanogr.*, **25**, 122-137, 1995.
- Alexander, M.A., and C. Penland, Variability in a mixed layer model of the upper ocean driven by stochastic atmospheric surface fluxes, *J. Climate*, **9**, 2424-2442, 1996.
- Alexander, M.A., and J.D. Scott, Surface flux variability over the North Pacific and North Atlantic Oceans, *J. Climate*, **10** (11), 2963-2978, 1997.
- Alexander, M.A., and J. D. Scott, Web-based atlas of climatology and variability in the GFDL R30S14 GCM., [Available on-line from <http://www.cdc.noaa.gov/gfdl/>], 2000.

- Anderson, S. P., R. A. Weller and R. B. Lukas 1996: Surface buoyancy forcing and the mixed layer of the western Pacific warm pool. *J. Climate*, **9**, 3056-3085.
- Barsugli, J.J., Idealized models of intrinsic midlatitude atmosphere-ocean interaction., Ph.D. thesis, University of Washington, [Available on line from <http://www.cdc.noaa.gov/~jjb/thesis.html>.], 1995.
- Barsugli, J.J., and D.S. Battisti, The basic effects of atmosphere-ocean thermal coupling on midlatitude variability., *J. Atmos. Sci.*, **55** (4), 477-493, 1998.
- Battisti, D.S., U. S. Bhatt, and M.A. Alexander, A modeling study of the interannual variability in the wintertime North Atlantic Ocean, *J. Climate*, **8** (12), 3067-3083., 1995.
- Bhatt, U.S., M. A. Alexander, D. S. Battisti, D. D. Houghton, and L.M. Keller, Atmosphere-ocean interaction in the North Atlantic: near-surface climate variability, *J. Climate*, **11**, 1615-1632, 1998.
- Bjerknes, J., Atlantic air-sea interaction, *Adv. in Geophys.*, **20**, 1-82, 1964.
- Blade, I., The influence of midlatitude coupling on the low frequency variability of a GCM. Part I: No tropical SST forcing, *J. Climate*, **10**, 2087-2106, 1997.
- Bryan, F. O., Climate drift in a multi-century integration of the NCAR Climate System Model, *J. Climate*, **11**, 1455-1471, 1998.
- Camp, N.T., and R.L. Elsberry, Oceanic thermal response to strong atmospheric forcing, II, the role of one-dimensional processes, *J. Phys. Oceanogr.*, **8**, 215-224, 1978.
- Cayan, D.R., Latent and sensible heat flux anomalies over the northern oceans: driving the sea surface temperature, *J. Phys. Oceanogr.*, **22**, 859-881, 1992.
- Clark, N.E., Specification of sea surface temperature anomaly patterns in the eastern North Pacific, *J. Phys. Oceanogr.*, **2**, 391-404, 1972.
- Davis, R.E., R. Deszoeke, D. Halpern, and P. Niiler, Variability in the upper ocean during MILE. Part I: The heat and momentum balances, *Deep Sea Research*, **28**, 1427-1451, 1981.
- Delworth, T., North Atlantic interannual variability in a coupled ocean-atmosphere model, *J. Climate*, **9** (10), 2356-2375, 1996.
- Deser, C., and M.S. Timlin, Atmosphere-Ocean interaction on weekly time scales in the North Atlantic and Pacific, *J. Climate*, **10** (3), 393-408, 1997.
- Dickson, R.R., J.R.N. Lazier, J. Meincke, P.B. Rhines, and J. Swift, Long-term coordinated changes in the convective activity of the North Atlantic, *Progress in Oceanography*, **38**, 241-295, 1996.
- Elsberry, R.L., and R.W. Garwood, Numerical ocean prediction models-goal for the 1980s, *Bull. Amer. Meteor. Soc.*, **61**, 1556-1566, 1980.
- Favorite, F., and D.R. McLain, Coherence in transpacific movements of positive and negative anomalies of sea surface temperature, 1953-1960, *Nature*, **244**, 139-143, 1973.
- Frankignoul, C., Sea surface temperature anomalies, planetary waves, and air-sea feedback in the middle latitudes, *Rev. Geophys.*, **23**, 357-390, 1985.
- Frankignoul, C., and R.W. Reynolds, Testing a dynamical model for mid-latitude sea surface temperature anomalies, *J. Phys. Oceanogr.*, **13**, 1131-1145, 1993.
- Garratt, J.R., A.J. Pratta, L.D. Rotstayn, and S. Cusack, The surface radiation budget over oceans and continents, *J. Climate*, **11**, 1951-1968, 1998.
- Garwood, R.W., An oceanic mixed layer model capable of simulating cyclic states, *J. Phys. Oceanogr.*, **7**, 455-468, 1977.
- Gascard, J.-C., and R.A. Clarke, The Formation of Labrador Sea Water. Part II: Mesoscale and smaller processes, *J. Phys. Oceanogr.*, **13**, 1779-1797, 1983.
- Gaspar, P., Modeling the seasonal cycle of the upper ocean, *J. Phys. Oceanogr.*, **18**, 161-180, 1988.
- Gaspar, P., Y. Gregoris, R. Stull, and C. Boisser, Long-term simulations of upper ocean vertical mixing using models of different types., in Small-scale turbulence and mixing in the ocean, edited by N.J.C.J.a.B.M. Jamart, pp. 169-184, Elsevier, Amsterdam, 1988.

- Gill, A.E., and P.P. Niiler, The theory of the seasonal variability in the ocean, *Deep Sea Res.*, **20**, 141-177, 1973.
- Gill, A.E., and J.S. Turner, A comparison of seasonal thermocline models with observations, *Deep-Sea Res.*, **23**, 391-401, 1976.
- Gordon, C., and M. Bottomley, The parameterization of the upper ocean mixed layer in coupled ocean-atmosphere models, in *Coupled Ocean-Atmosphere Models*, edited by J.C.J. Nihoul, pp. 613-635, Elsevier Oceanography series, New York, 1985.
- Gordon, C.T., and W. Stern, A description of the GFDL global spectral model, *Mon. Wea. Rev.*, **110**, 625-644, 1982.
- Gordon, H.B. and S.P. O'Farrell, Transient climate change in the CSIRO coupled model with dynamical sea ice. *Mon. Wea. Rev.*, **125**, 875-905, 1997.
- Halliwell, G.R., and D.A. Mayer, Frequency response properties of forced climatic SST anomaly variability in the North Atlantic, *J. Climate*, **9** (12, Part III), 3575-3587, 1996.
- Haney, R.L., A numerical case study of the development of large-scale thermal anomalies in the central North Pacific Ocean, *J. Phys. Oceanogr.*, **10**, 541-556, 1980.
- Haney, L.R., B.H. Houtman, and W.H. Little, The relationship between wind and sea surface temperature anomalies in the mid-latitude North Pacific Ocean, *Atmos. Ocean*, **21**, 168-186, 1983.
- Hanson, H.P., COADS as a diagnostic modeling tool: air-sea interaction and the role of the deep ocean circulation in climate change, in *Proceedings of the International COADS Workshop*, edited by K.W. Henry Diaz, Scott Woodruff, pp. 315-322, NOAA, Boulder, CO, 1992.
- Hasselmann, K., Stochastic climate models., *Tellus*, **28**, 473-485, 1976.
- Herterich, K., and K. Hasselmann, Extraction of mixed layer advection velocities, diffusion coefficients, feedback factors and atmospheric forcing parameters from the statistical analysis of North Pacific SST anomaly fields. *J. Phys. Oceanogr.*, **17**, 2145-2156, 1987.
- Horel, J.D., and J.M. Wallace, Planetary-scale atmospheric phenomena associated with the interannual variability of sea surface temperature in the equatorial Pacific, *Mon. Wea. Rev.*, **109**, 813-829, 1981.
- Hsuing, J., Estimates of global oceanic meridional heat transport, *J. Phys. Oceanogr.*, **15**, 1405-1413, 1985.
- Inui, T., K. Takeuchi, and K. Hanawa, A numerical investigation of the subduction process in response to an abrupt intensification of the westerlies. *J. Phys. Oceanogr.*, **29**, 1993-2015, 1999.
- Iwasaka, N., and J.M. Wallace, Large scale air sea interaction in the Northern Hemisphere from a view point of variations of surface heat flux by SVD analysis., *J. Meteor. Soc. Japan*, **73** (4), 781-794, 1995.
- Jacob, W.J., Numerical semiprediction of monthly mean sea surface temperature, *J. Geophys. Res.*, **72**, 1681-1689, 1967.
- Kantha, L.H., and C.A. Clayson, An improved mixed layer model for geophysical applications, *J. Geophys Res.*, **99** (c12), 25235-25266, 1994.
- Kiehl, J., Simulation of the tropical Pacific warm pool with the NCAR Climate System Model., *J. Climate*, **11**, 1342-1355, 1998.
- Kim, J., A generalized bulk model of the oceanic mixed layer, *J. Phys. Oceanogr.*, **6**, 686-695, 1976.
- Kraus, E.B., Merits and defects of different approaches to mixed layer modelling, in *Small-scale turbulence and mixing in the ocean*, edited by N.J.C.J.a.B.M. Jamart, pp. 37-50, Elsevier, Amsterdam, 1988.
- Kumar, A., and M.P. Hoerling, Annual cycle of Pacific North America seasonal predictability associated with different phases of ENSO., *J. Climate*, **11**, 3295-3308, 1998.
- Ladd, C. and L. Thompson, (1999): Formation mechanisms for North Pacific central and eastern subtropical mode waters. *Journal of Physical Oceanography*, **30**, 868-887.

- Lanzante, J.R., and R.P. Harnack, An investigation of summer sea surface temperature anomalies in the eastern North Pacific Ocean, *Tellus*, **35A**, 256-268, 1983.
- Large, W.G., J.C. McWilliams, and S.C. Doney, Oceanic vertical mixing: a review and a model with a nonlocal boundary layer parameterization, *Rev. Geophys.*, **32**, 363-404, 1994.
- Large, W.G., J.C. McWilliams, and P.P. Niiler, Upper ocean thermal response to strong autumnal forcing over the Northeast Pacific, *J. Phys. Oceanogr.*, **16**, 1524-1550, 1986.
- Lau, N.-C., and M.J. Nath, The role of the 'atmospheric bridge' in linking tropical Pacific ENSO events to extratropical SST anomalies., *J. Climate*, **9** (9), 2036-2057, 1996.
- Ledwell, J.R., A.J. Wilson, and C.S. Low, Evidence for slow mixing across the pycnocline from an open-ocean tracer release experiment, *Nature*, **364**, 701-703, 1993.
- Le Treut, H., J.Y. Simonot, and M. Crepon, A model for the sea-surface temperature and heat content in the North Atlantic Ocean, in *Coupled Ocean-Atmosphere Models*, edited by J.C.J. Nihoul, pp. 439-446, Elsevier, Amsterdam, 1985.
- Lukas, R. and E. Lindstrom, The mixed layer of the western equatorial Pacific Ocean, *J. Geophys. Res.*, **96**, 3343-3357, 1991.
- Luksch, U., Simulation of North Atlantic low frequency variability., *J. Climate*, **9** (9), 2083-2092, 1996.
- Luksch, U., and H. von Storch, Modeling the low-frequency sea surface temperature variability in the North Pacific, *J. Climate*, **5**, 893-906, 1992.
- Manabe, S., and D.G. Hahn, Simulation of atmospheric variability, *Mon. Wea. Rev.*, **109**, 2260-2286., 1981.
- Manabe, S., and R.J. Stouffer, Two stable equilibria of a coupled ocean-atmosphere model, *J. Climate*, **1**, 841-866, 1988.
- Marshall, J. C., A.J.G. Nurser, and R.G. Williams, Inferring the subduction rate and period over the North Atlantic, *J. Phys. Oceanogr.*, **23**, 1315-1329, 1993.
- Martin, P.J., Simulation of the mixed layers at OWS November and Papa with several models, *J. Geophys. Res.*, **90**, 903-916, 1985.
- Miller, A.J., D.R. Cayan, T.P. Barnett, N.E. Graham, and J.M. Oberhuber, Interdecadal variability of the Pacific Ocean: model response to observed heat flux and wind stress anomalies, *Climate Dyn.*, **10**, 287-302, 1994.
- Mitchell, T.P., and J.M. Wallace, ENSO seasonality :1950-78 versus 1979-92., *J. Climate*, **9**, 3149-3161, 1996.
- Miyakoda, K., and A. Rosatil, The variation of sea surface temperature in 1976 and 1977 2. The simulation with mixed layer models, *J. Geophys. Res.*, **89**, 6533-6542, 1984.
- Moisan, J.R., and P.P. Niiler, The seasonal heat budget of the North Pacific: net heat flux and heat storage rates (1950-1990), *J. Phys. Oceanogr.*, **28** (3), 401-421, 1998.
- Monterey, G.I., and S. Levitus, *Climatological Cycle of Mixed Layer Depth in the World Ocean*, 5 pp., 87 figs. pp., U.S. Gov. Printing Office, NOAA NESDIS, Wash., D.C, 1997.
- Moore, A. M. and H. B. Gordon, An investigation of climate drift in a coupled atmosphere-ocean-sea ice model, *Climate Dyn.*, **10**, 81-95, 1994.
- Namias, J., Recent seasonal interactions between North Pacific waters and the overlying atmospheric circulation, *J. Geophys. Res.*, **64**, 631-646, 1959.
- Namias, J., Large-scale air-sea interactions over the North Pacific from summer (1962) through the subsequent winter, *J. Geophys. Res.*, **68**, 6171-6186, 1963.
- Namias, J., Macroscopic association between mean monthly sea surface temperature and the overlying winds, *J. Geophys. Res.*, **70**, 2307-2318, 1965.
- Namias, J., Experiments in objectively predicting some atmospheric and oceanic variables for the winter of 1971-1972, *J. Appl. Meteor.*, **11**, 1164-1174, 1972.
- Namias, J., and R.M. Born, Temporal coherence in North Pacific sea-surface temperature patterns, *J. Geophys. Res.*, **75**, 5952-5955, 1970.

- Namias, J., and R.M. Born, Further studies of temporal coherence in North Pacific sea surface temperatures, *J. Geophys. Res.*, **79**, 797-798, 1974.
- New, A. L., R. Bleck, Y. Jia, R. Marsh, M. Huddleston, and S. Barnard, An isopycnic model study of the North Atlantic. Part I: Model experiment, *J. Phys. Oceanogr.*, **25**, 2667-2699, 1995.
- Niiler, P.P., and E.B. Kraus, One dimension models of the upper ocean, in *Modeling and Prediction of Upper Layers of the Ocean*, edited by E.B. Kraus, pp. 143-172, Pergamon Press, 1977.
- Norris, J.R., and C. Leovy, Interannual variability in stratiform cloudiness and sea surface temperature., *J. Climate*, **7**, 1915-1925., 1994.
- Norris, J.R., Y. Zhang, and J.M. Wallace, Role of clouds in summertime atmosphere-ocean interactions over the North Pacific, *J. Climate*, **11**, 2482-2490, 1998.
- Oberhuber, J. M., Simulation of the Atlantic circulation with a coupled sea ice-mixed layer-isopycnal general circulation model. Part II: model experiment, *J. Phys. Oceanogr.* **23**, 830-845, 1993.
- Ostrovskii, A. G. and L. I. Piterbarg, Inversion of Upper Ocean Temperature Time Series for Entrainment, Advection, and Diffusivity, *J. Phys. Oceanogr.*, **30**, 201-204, 2000.
- Paulson, C., A., and J.J. Simpson, Irradiance measurements in the upper ocean, *J. Phys. Oceanogr.*, **7**, 952-956, 1977.
- Price, J.F., R.A. Weller, and R. Pinkel, Diurnal cycling: observations and models of the upper ocean response to diurnal heating, cooling, and wind mixing, *J. Geophys. Res.*, **91** (c7), 8411-8427, 1986.
- Salmon, R., and M.C. Hendershott, Large scale air-sea interactions with a simple general circulation model, *Tellus*, **28**, 228-242, 1976.
- Saravanan, R., Atmospheric low frequency variability and its relationship to midlatitude SST variability: studies using the NCAR climate system model, *J. Climate*, **11**, 1386-1404, 1998.
- Sausen, R., K. Barthel, and K. Hasselmann, Coupled ocean-atmosphere models with flux correction, *Climate Dyn.*, **2**, 145-163, 1988.
- Schneider, N., A. J. Miller, M.A. Alexander, and C. Deser, Subduction of decadal north Pacific temperature anomalies: observations and dynamics, *J. Phys. Oceanogr.*, **29**, in press, 1999.
- Seager, R., Y. Kushnir and M.A. Cane, On heat flux boundary conditions for ocean models. *J. Phys. Oceanogr.*, **25**, 3219-3230, 1995.
- Shinoda, T., and H.H. Hendon, Mixed layer modeling of intraseasonal variability in the tropical west Pacific, *J. CLimate*, **11** (10), 2668-2685, 1998.
- Simonot, J.Y., H.L. Treut, and M. Crepon, A thermodynamic model of the global sea-surface temperature and mixed layer depth, in *Small-Scale Turbulence and Mixing in the Ocean*, edited by J.C.J. Nihoul, and B.M. Jamart, pp. 123-139, Elsevier, New York, 1988.
- Smith, T.M., R.W. Reynolds, R.E. Livezey, and D.C. Stokes, Reconstruction of historical sea surface temperatures using empirical orthogonal functions., *J. Climate*, **9**, 1403-1420, 1996.
- Webster, P.J., and R. Lukas, TOGA COARE: the Coupled Ocean-Atmosphere Response Experiment, *Bull. Amer. Met. Soc.*, **73** (9), 1377-1416, 1992.
- White, W., B., R. Bernstein, G. McNally, S. Pazan, and R. Dickson, The thermocline response to transient atmospheric forcing in the interior midlatitude North Pacific 1976-1978, *J. Phys. Oceanogr.*, **10**, 372-384, 1980.
- Wilkin, J.L., J.V. Mansbridge, and J.S. Godfrey, Pacific Ocean heat transport at 24 degrees N in a high-resolution global model, *J. Phys. Oceanogr.*, **25** (10), 2204-2214.
- Woods, J. D., The physics of thermocline ventilation, in *Coupled ocean-atmosphere models*, Edited by J. C. J. Nihoul, pp. 543-590, Elsevier, Amsterdam, 1985.
- Yu, L., and P. Malanotte-Rizzoli, Inverse modeling of seasonal variations in the North Atlantic Ocean, *J. Phys. Oceanogr.*, **28** (5), 902-922, 1998.